Integration of fluid-invasive, scattering, and imaging methods in resolving pore structures in coal and shale

Kumar, Shubham; Chandra, Debanjan; Hazra, Bodhisatwa; Vishal, Vikram; Ranjith, Pathegama Gamage; Das, Anwesa; Ahuja, Mayank; Ghosh, Sayan

DOI
10.1016/j.fuel.2025.135185

Publication date
2025

Document Version
Final published version

Published in
Fuel

Citation (APA)
Kumar, S., Chandra, D., Hazra, B., Vishal, V., Ranjith, P. G., Das, A., Ahuja, M., & Ghosh, S. (2025). Integration of fluid-invasive, scattering, and imaging methods in resolving pore structures in coal and shale. *Fuel*, *395*, Article 135185. https://doi.org/10.1016/j.fuel.2025.135185

Fuel 395 (2025) 135185

Contents lists available at ScienceDirect

Fuel

journal homepage: www.elsevier.com/locate/fuel

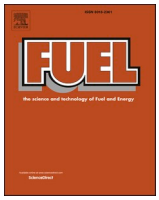

Full Length Article

Integration of fluid-invasive, scattering, and imaging methods in resolving pore structures in coal and shale

Shubham Kumar [a,b], Debanjan Chandra [c,d], Bodhisatwa Hazra [e], Vikram Vishal [a,f,g,*], Pathegama Gamage Ranjith [b], Anwesa Das [h], Mayank Ahuja [h], Sayan Ghosh [h]

[a] Computational and Experimental Geomechanics Laboratory, Department of Earth Sciences, Indian Institute of Technology Bombay, Mumbai 400076, India
[b] Department of Civil Engineering, Faculty of Engineering, Monash University, Clayton, Melbourne, Victoria 3800, Australia
[c] Department of Geoscience and Engineering, Delft University of Technology, 2628 CN Delft, the Netherlands
[d] Department of Geoscience (IGV), Norwegian University of Science and Technology, S. P. Andersens veg 15A, 7031 Trondheim, Norway
[e] CSIR- Central Institute of Mining and Fuel Research, Barwa Road Campus, Dhanbad 826015, India
[f] DST-National Centre of Excellence in Carbon Capture and Utilization, Indian Institute of Technology Bombay, Mumbai 400076, India
[g] Interdisciplinary Programme in Climate Studies, Indian Institute of Technology Bombay, Mumbai 400076, India
[h] Central Mine Planning & Design Institute Limited (CMPDIL), Ranchi, Jharkhand 834031, India

ARTICLE INFO

Keywords:
Coal and Shale
Gas Adsorption
SEM Imaging
X-ray Scattering
Mercury Intrusion Porosimetry
Pore Connectivity

ABSTRACT

In this study, coal and shale samples were collected from the gas-rich Barakar Formations and investigated using various analytical and imaging methods, to quantify their pore attributes. The results indicate that coal contains an abundance of nanopores that occur in clusters, along with evidence of microfractures in its structure, as observed through scanning electron microscopy (SEM). The accessible micropore surface area (SA) of coal samples is around 2.5 times higher than that of shale samples, while the total mesopore SA in coal is around half that of shales. However, the average pore width of coal samples is approximately 0.82 times that of shale samples. These findings suggest that a higher percentage of organic carbon in coal contributes to an abundance of organic pores, which results in greater porosity in coal samples when compared to shale. The total SA determined by gas adsorption for the entire spectrum of pore sizes in coal is around two times that of shale. Interestingly, despite the difference in the pore SA and the pore volume, the pore surface roughness in the studied coals is almost equal to or slightly higher than that of shales. The study observations show that the total organic carbon and mineral composition in coal and shale play little influence on the degree of pore connectivity. The degree of pore connectivity for the coal samples varies from 0.4–0.93, whereas for shale samples it ranges from 0.50–0.82. This study provides analytical insights into the pore structure of coal and shale collected from the same reservoir by considering factors such as depth, mineralogical content, and surface roughness. During CO_2 injection, coal and shale reservoirs may experience swelling induced stress changes, potentially impacting their mechanical stability. Thus, this study provides insight into estimating the gas-storage capacities of both coal and shale reservoirs and aims to optimise the gas adsorption and maintain structural integrity. This approach ensures the long-term feasibility of implementing Enhanced Coalbed Methane (ECBM) recovery and shale gas recovery in other gas basins.

Abbreviations: **P** (in torr), Vapor Pressure; $\mathbf{P_o}$ (in torr), Condensation Pressure of N_2 and CO_2 at 77 K and 273.15 K, respectively; **V** (in cc/g), Volume of N_2 - CO_2 gas adsorbed on the adsorbent at an equilibrium pressure (P/Po); $\mathbf{V_m}$ (in cc/g), Gas Volume at monolayer adsorption; **C**, Power-law exponent depending on Ds; $\mathbf{T_{max}}$, Thermal Maturity of coal and shale samples; **β**, Matrix Compressibility; $\mathbf{V_c}$, Volume of the coal matrix in m^3 and; $\mathbf{P_{Hg}}$, Mercury injection pressure (in MPa); $\Delta\mathbf{V}_{Hg}$, Volume of the total intruded mercury (cc/g); $\Delta\mathbf{V}_{pore}$, pore filling volume (cc /g) using LPGA method; $\Delta\mathbf{V}_o$, Coal matrix deformation volume (cc/g).

* Corresponding author at: Computational and Experimental Geomechanics Laboratory Department of Earth Sciences, Indian Institute of Technology (IIT) Bombay Powai, Mumbai 400076, India.
E-mail address: v.vishal@iitb.ac.in (V. Vishal).

https://doi.org/10.1016/j.fuel.2025.135185
Received 28 January 2025; Received in revised form 14 March 2025; Accepted 21 March 2025
Available online 2 April 2025

1. Introduction

The pore structure in unconventional resources such as shale [1,2] and coal formations [3,4] plays an important role in energy transition and mitigating carbon emissions. The complex nanoscale pore structure and their pore connectivity in unconventional gas reservoirs (UGR) significantly influences the migration and transport of hydrocarbons (HCs) within these reservoirs. Understanding pore characteristics, including pore volume (PV), pore width (PW), and surface area (SA) in coal and shale, is essential in investigating methods of gas exploration and storage in organic-rich strata [5,6]. Coal formations exhibit a complex pore structure, which is often modelled using dual porosity and dual permeability approximations [7,8]. Coal and shale matrices are composed of micropores (<2 nm) and mesopores (2–50 nm) [9], while the pores in natural fractures are categorised as macropores (>50 nm) [10]. Coal and shale are fine-grained sedimentary rocks primarily consisting of clay minerals (~ 57 %) [11], quartz, and carbonates. The pore structure is primarily made up of micro- and mesopores, which contribute significantly to subsurface gas storage [12,13]. Shale formations act as both source rocks and seals for oil & gas traps, highlighting their importance in gas exploration. The depositional patterns of coal and shale are distinctly different in terms of the organic matter (OM) content and environmental conditions. Coal typically forms in low-lying swampy conditions, which are rich in terrestrial plant-based organic matter [14]. In contrast, shale formation is linked with low-energy sedimentation and consist of a mix of terrestrial and aquatic organic matter. This disparity shows the complex interplay of geological and biological factors in sedimentary processes. Variations in conditions such as the pH and microbial activity lead to differences in the chemical composition, physical properties, and overall quality of coal and shale formations [15], which, in turn, affect their gas storage potential. Gases in the pores of these sedimentary rocks are primarily stored through physisorption. Most of the gas is adsorbed onto the inner walls of OM and clay minerals (CM), and a smaller proportion is stored as absorbed gas or free gas within the pores and natural fractures. Several studies [16–19] have been conducted that focus on the assessment of the pore attributes of coal and shale. Wang et al. [20] shows that coal and shale have different pore structures that result in different gas adsorption capacities. Zhang et al.[21] emphasize that physisorption shows a crucial role in determining the methane sorption capacity in both CM and OM in shale. Changes in pore characteristics are influenced by depth, which also affect rock-gas interaction during the sorption process in UGRs. The OM content, with its high SA and PV, is imperative to quantify for gas exploration and storage in UGRs. It is also a key factor in determining porosity networks in these reservoirs [22,23]. Several authors [24,25] demonstrated that illite has the highest methane adsorption capacity and its hydrophilic properties influence this. Nevertheless, it is essential to explore the differences between coal and shale pore structures to identify gas occurrence characteristics accurately.

In recent decades, considerable attention has focused on UGRs, with particular interest in enhancing coal bed methane (CBM) [26,27] and shale gas (SG) recovery [28,29] through CO_2 sequestration. Various experimental techniques [30–34] and numerical simulations [35–37] have been used to explore the technical feasibility of UGR. Experimental methods, including direct techniques such as field-emission gun scanning electron microscopy (FEG-SEM) and indirect methods such as low-pressure gas adsorption (LPGA), small-angle neutron/x-ray scattering (SANS/SAXS) and mercury intrusion capillary porosimetry (MICP) as shown in Fig. 1 as, are routinely employed to measure nanoscale pores in coal and shale.

Pore surface roughness in coal and shale formations is a critical parameter that governs fluid-flow mechanisms and gas-adsorption kinetics. Surface roughness is quantified using the fractal dimension (D_f), which is a measure of self-similarity in Euclidean objects across different scales. The D_f value provides insights into the complexity of pore structures in coal and shale. Higher D_f values indicate more complex structures, particularly in macropores. The OM content, mineral composition, and pore morphology significantly influence fractal behaviour, with total organic carbon (TOC) content showing a constructive correlation with mesopore fractal attributes [39]. The values of D_f in porous media can range from 2 (smooth surfaces) to 3 (rough surfaces). Furthermore, understanding the adsorption capacity and the fractal behaviour of coal and shale in the aspect of CO_2 sequestration is crucial to provide a theoretical possibility of implementing SG and CO_2-ECBM recovery [40].

The study aims to characterise the pore structure of unconventional rock formations from the prolific gas-bearing Korba Basin, India specifically the Barakar Formation. We investigate a broad range of nanoscale pores, including micro- to macropores, using techniques such as SEM, LPGA, MICP, and SAXS. Furthermore, this study explores the correlation between pore attributes and geological parameters, including depth, organic richness, mineral composition, and surface irregularity. These parameters affect the pore structure in both coal and shale. This article will enhance our understanding of gas adsorption

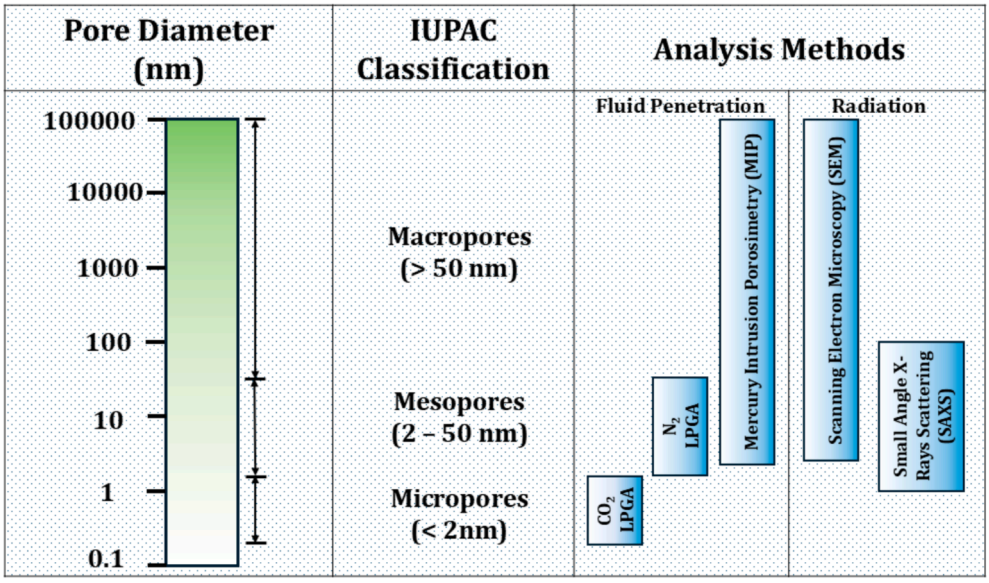

Fig. 1. Various methods applied to determine hierarchical pore characteristics of coal and shale samples [38].

capacities and migration pathways, which would contribute to carbon neutrality efforts and aid the evaluation of storage capacities in other gas-rich basins.

2. Methodology

2.1. Sampling area

The samples were collected from the Barakar Formation of the Korba Basin, which is located in central India as shown in Fig. 2. The Korba Basin contains one of the largest coal reserves in the country, with estimated reserves of approximately 3,042.37 million tonnes [41]. The samples were collected from the Kartala Block, which is situated in the south-central region of the Son–Mahanadi River valley. The basin covers an area of 530 km^2, lying between the latitudes, 22°01′– 23°01′ N, and longitudes, 82°01′– 83°07′ E. The Hasdo River flows from the north to the south and eventually joins the Mahanadi River, while the Mand River flows through along the eastern boundary of the basin, serving as a

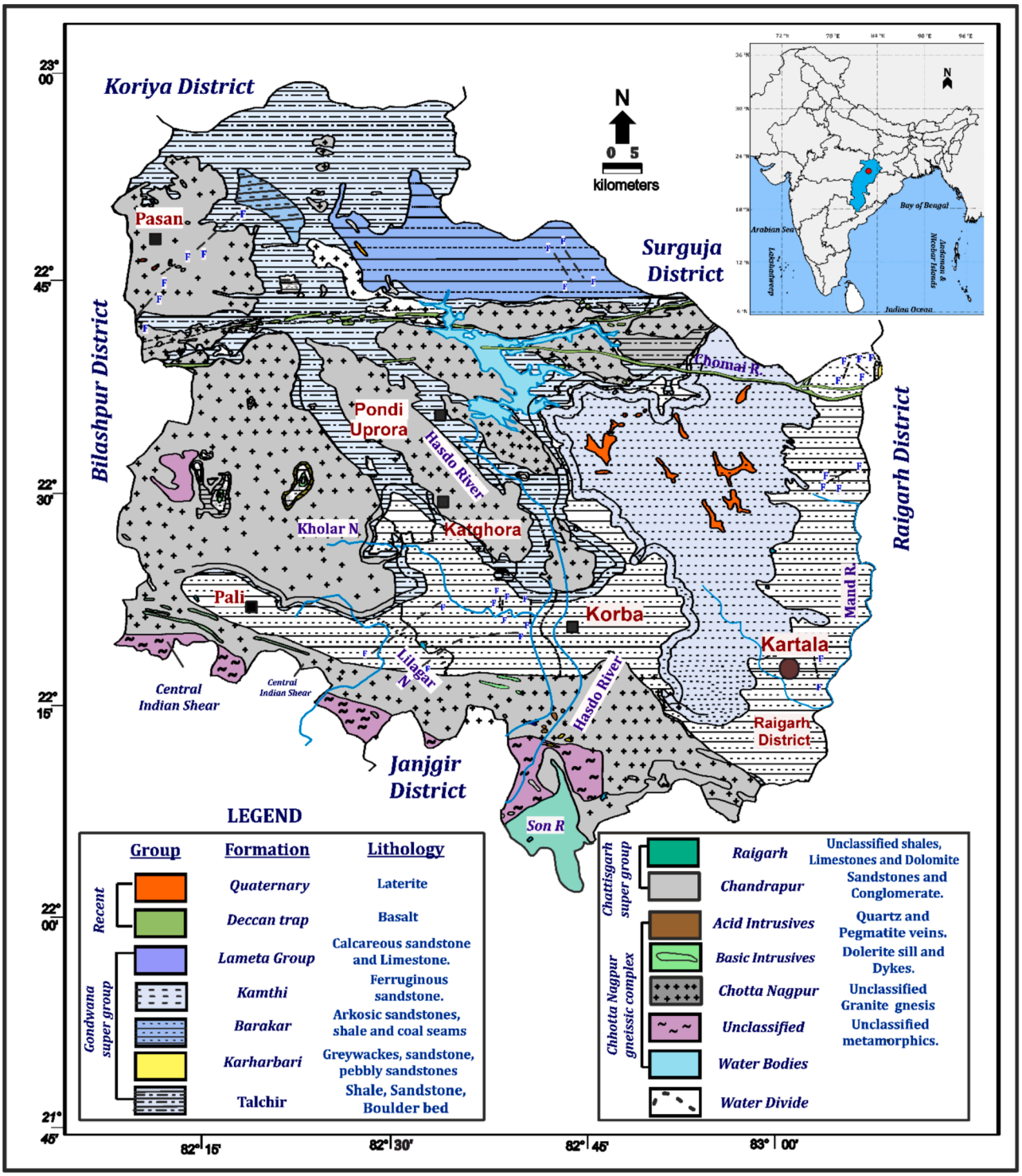

Fig. 2. Detailed stratigraphy of the Korba Basin. (Reproduced from Kumar et al. [42]). The location of the sample collection is marked by the brown circle (Kartala Block).

tributary to the Mahanadi.

The Gondwana Supergroup in this region is represented by the Barakar, Karharbari, Kamthi, and Talchir formations, with the Barakar Group dominating much of the Korba–Gondwana Basin. The Barakar Formation predominantly comprises medium- to coarse-grained arkosic sandstones, pebble beds, conglomerates, and shales interbedded with coal seams. The sandstones are typically feldspathic and ferruginous. Fractures are often observed in the coal facies, which are thin to moderately thick. Several authors [43–45] have provided detailed descriptions of the tectonics and the stratigraphy of the Korba region.

2.2. Sample description

Coal samples from the Korba Basin were collected from depths ranging between 170 and 711 m and labelled as KB 1 to KB 8, while shale samples were labelled as SH 1 to SH 5, as shown in Table 1. To prevent contamination, the core samples were stored in airtight zipper bags. The samples were pulverized using an agate mortar and screened with a copper sieve to retain a grain size of < 75 μm (~200 mesh) for the experiments [29,46]. Coarse samples with dimensions of < 1 mm^3 [17] were dried at a temperature of 100 °C for about 6 h before using it for the MICP method, while small flakes (~1 mm thick) with smooth and flat surfaces were prepared for FEG-SEM imaging.

2.3. Mineral content and thermal maturity

The mineral content in the samples was determined using PANalytical's X'Pert Pro instrument. The instrument operates at a maximum voltage of 40 kV with a Cu cathode. Coal samples were heated to approximately 300 °C in an oven at a rate of 10 °C/min for a duration of 6–8 h [47–49]. This heat treatment removes OM, which enhances the sharpness of intensity peaks and improves the accuracy of mineral composition measurements in coal. Approximately 5–10 mg of each pulverized sample was uniformly loaded onto the sample holder. The peaks were detected within a scanning range (2θ) of 5°–70° with a scanning step size of 0.0130°/s. The X-ray diffractogram patterns were analysed using the HighScore Plus software suite.

The organic richness in unconventional resources shows a critical role in gas production and storage through UGR. Rock-eval pyrolysis is an analytical technique used to evaluate the HC source-rock potential of OM in geological samples such as coal and shale. It provides qualitative and quantitative information on thermal maturity, kerogen types, and HC generation, which are vital in assessing source rocks. Approximately 5–10 mg of pulverized samples (around 200 mesh grain size) was analysed to determine the TOC using the Rock-Eval 6 instrument. Initially, the pulverised samples were placed in the pyrolysis chamber and heated isothermally to 300 °C. The HCs that were released during the process were detected by a Flame Ionization Detector (FID) and were carried by N_2 gas and logged as 'S1′ peak. Subsequently, the samples were heated from 300 °C to 650 °C at a heating rate of 25 °C/min. During this stage, the OM in the samples began decomposing into HCs, which were again carried by N_2 gas, detected by the FID, and noted as an 'S2′ peak. Furthermore, the temperature at which maximum HC generation occurs at the S2 stage was designated as 'Tmax', which served as an indicator of the thermal maturity of the OM in the samples. Additionally, oxygen-rich compounds in the OM decomposed during the pyrolysis stage, releasing CO and CO_2, which were detected by an infrared cell and noted as the 'S3′ peak. The total carbon released during the S1, S2, and S3 stages is referred to as Pyrolysable Carbon (PC). Following pyrolysis, the samples were transferred to an oxidation chamber, where they were heated under oxidizing conditions. The Residual Carbon (RC) that remains after this process was measured. The TOC is calculated by computing the PC and the RC. To assess the thermal maturity of the samples, a modified van Krevelen plot (Hydrogen Index [HI] versus Oxygen Index [OI]) was employed Eqs. (1) and (2).

$$\mathrm{HI} = [(\frac{\mathrm{S2}}{\mathrm{TOC}}) \text{ x } 100] \quad (1)$$

$$\boldsymbol{OI} = [(\frac{\mathrm{S3}}{\mathrm{TOC}}) \text{ x } 100] \quad (2)$$

2.4. High-resolution imaging method (FEG-SEM)

FEG-SEM is widely used to visualise and observe high-resolution images of pore structures and connectivity at the nanoscale [50]. It plays a critical role in qualitatively determining the microstructures of solid samples such as coal and shale. Initially, the samples were dried at a temperature of 105 °C for at least 12 h to remove any moisture and volatile content. Flat flakes with smooth surface reliefs on both sides were mounted on sample holders using double-sided carbon adhesive tape. To enhance surface conductivity, a thin platinum film (~10 nm) was sputtered onto the samples. High-resolution images were captured at various magnifications to identify pores across different scales. This study utilized a JEOL JSM-7600F FEG-SEM equipped with an in-lens Schottky field-emission gun, which operated at a maximum voltage of 30 kV. The pixel density for the coal samples ranged between 0.018 and 12.66 pixels/μm, while for the shale samples, it ranged between 0.84 and 2.5 pixels/μm.

2.5. Low-pressure gas adsorption (LPGA)

LPGA method is widely accepted to determine pore characteristics in porous media, including coal and shale samples. It is a fluid-invasive technique that uses CO_2 and N_2 gases as probes for micropores and

Table 1
Mineral composition of coal and shale samples from Korba Basin. (All composition is in wt. percentage).

Sample ID	Rock Type	Depth (m)	Quartz	Clay Minerals		Feldspar	Muscovite	Sericite	Other
				Illite	Kaolinite				
KB 1	Coal	170	32	3	56	1	0	8	0
KB 2	Coal	194	14	2	74	0	0	10	0
KB 3	Coal	255	8	6	80	0	0	6	0
KB 4	Coal	285	36	0	64	0	0	0	0
KB 5	Coal	306	7	6	58	6	8	0	15 (Microcline)
KB 6	Coal	364	17	14	69	0	0	0	0
KB 7	Coal	534	22	23	26	13	16	0	0
KB 8	Coal	711	32	0	68	0	0	0	0
SH 1	Shale	182	43	0	39	0	15	0	3 (Siderite)
SH 2	Shale	289	34	0	52	11	3	0	0
SH 3	Shale	329	34	0	59	0	7	0	0
SH 4	Shale	491	43	0	43	0	1	13	0
SH 5	Shale	582	29	5	44	0	22	0	0

mesopores, respectively, in porous samples. In this study, 2–3 g of both coal and shale powderswere analysed using a single-station Quantachrome Autosorb iQ physisorption instrument, were used in the experiments. Prior to the experiment, the samples were degassed at a temperature of 110 °C for at least 12 h at a pressure of 10^{-4} torr to remove moisture and lighter hydrocarbons. A similar degassing procedure has been employed by several researchers [29,46,51]. Micropores in coal and shale are commonly probed using CO_2 gas due to their small kinetic diameter and high diffusion rate. The CO_2 gas adsorption is conducted at 273.15 K with a relative pressure (P/P_0) that ranges from 0.0003 to 0.3, where P_0 is the condensation pressure for pure CO_2, which is 26,610 torr. From CO_2 adsorption isotherms, the micropore SA is determined using the Dubinin – Radushkevich (DR) equation, while the micropore volume is determined using the Dubinin – Astakhov (DA) method. The PSD is derived from the CO_2 adsorption isotherm using Density Functional Theory (CO_2-DFT). The N_2 adsorption isotherm is measured at – 196.3 °C (77 K) at a relative pressure (P/P_0) range of 0.01 to 0.99, where P_0 is the condensation pressure of nitrogen at 760 torr. In this context, N_2 gas is commonly used to evaluate mesopore volume and surface area due to its diatomic molecular structure, quadrupolar nature, and low chemical reactivity. The Brunauer–Emmett–Teller (BET) equation is used to determine the mesopore SA, while the total PV is determined using the Kelvin equation for both coal and shale samples. The combination of CO_2 and N_2 gas adsorption provides a comprehensive view across the micro- and mesopore ranges. Numerous studies [52,53] have demonstrated the effectiveness of using both CO_2 and N_2 adsorption for a wide spectrum of pore attributes. Density Functional Theory (DFT) is the standard approach for interpreting physisorption calculations and is widely accepted for analysing PSD. Unlike capillary condensation methods, the DFT is independent of such limitations. To address surface roughness, the Quenched Solid Density Functional Theory (QSDFT) model is applied to calculate the PSD while accounting for surface irregularities [29]. The QSDFT model can accurately provide a PSD of up to 40 nm and is more sensitive in the smaller mesopore range, whereas the Barrett–Joyner–Halenda (BJH) method measures a PSD of up to 200 nm and is more accurate for larger mesopores and macropores.

2.6. Mercury intrusion capillary porosimetry

Mercury Intrusion Capillary Porosimetry (MICP) is a fluid-invasive method that is used to determine pore connectivity in both coal and shale samples. This method provides detailed information about the pore structure, including the PSD, total PV, and SA, by measuring the volume of mercury that intrudes into the pores of a solid under increasing pressures of up to 60,000 psi (~ 414 MPa). The MICP method is suitable for characterising a broad range of pore sizes, from larger pores to smaller capillaries. Liquid mercury has unique properties that include its inability to wet most solid surfaces and its high density, which allows it to penetrate smaller pores effectively. During the procedure, sample chunks are placed into a penetrometer that is designed for low-porosity samples; the chunks are surrounded by liquid mercury. As the pressure increases, mercury intrudes into the pores, progressively filling voids. A higher intrusion pressure forces the mercury into the smaller pores. Pure mercury has a surface tension (Y) of 480.00 mN/m and a contact angle (θ) of 140°. In this research, experiments were performed using a Mercury Intrusion-Extrusion Pore-Size Analyzer (PoreMaster PM60) manufactured by Anton-Paar. The samples were heated to a temperature of 100 °C for at least 6 h to remove any moisture content that could otherwise introduce errors in the measurements [54,55]. The MICP instrument can measure pore sizes ranging from 0.0036 to 1000 μm. Pore properties such as the PV, SA, and PSD were calculated using the Washburn equation. The pressure required to fill pores of different sizes depends on the capillary forces and the curvature of the liquid–gas interface within the pores. The pressure at which mercury intrudes each pore size corresponds to the pore diameter. This method is based on the Kelvin equation, which relates intrusion pressure to pore size Eq. (3). The instrument records the volume of the mercury that intrudes into the sample as a function of the applied pressure. The total mercury intrusion volume determines the sample's total PV, while the pore throat radius is calculated using the Washburn equation [56–58]. This method relates the volume of mercury intrusion to the pressure and the contact angle.

$$r = \frac{-2Y\cos\theta}{P_{Hg}} \tag{3}$$

However, MICP has certain limitations. It is not suitable for samples that are sensitive to mercury intrusion. Additionally, in samples with very small or irregular pores, the experimental results may yield inaccuracies.

2.7. Small-angle X-ray scattering

Small-angle X-ray scattering (SAXS) is a non-destructive method used to analyse the pore structure of mesoporous materials. It quantifies pore characteristics over a wide range of length scales, from nanometers to millimeters. The method operates based on the principle of X-ray scattering, where each mineral component within the sample possesses a unique scattering length density (SLD). Variations in scattering arise due to chemical heterogeneity and differences in density and porosity within the sample. This study uses Xenocs SAS Xeuss 2.0 instrument with a 30 W GeniX3D Cu X-ray source that operates at 50 kV and 0.6 mA. The data was collected using an Eiger R 1 M detector, which is a high-resolution hybrid pixel photon-counting detector with a pixel size of ~ 75 μm. The software, Foxtrot, and Xsact, which were provided by Xenocs, were utilised for data acquisition. The distance for the sample-to-detector was set at approximately 6 m. Pulverised samples (< 75 μm) were packed and mounted within Kapton tape to ensure consistency in sample thickness. In the experimental setup, the scattering wave vector (Q) range was considered between 0.01 and 1.5 nm^{-1}. The transmission and the consequent X-ray intensity were normalised against the thickness of each sample. The SLD for each sample was determined using a weighted average of the bulk density and the SLD values of the mineral components. The matrix exhibited a near-uniform SLD, and a two-phase approximation was applied to interpret the scattering profiles of both coal and shale samples. This study uses the polydisperse spherical pore (PDSP) model to calculate the porosity and the PSD from the scattering data (I(Q) versus Q) based on the SAXS method. The PDSP model assumes that the calculated pore dimensions represent the average values across all orientations, with pores modelled as spheres. Detailed calculations are available in [59]. The raw data files were processed using the open-source MATSAS code in MATLAB [60].

3. Results

3.1. Mineralogy and thermal maturity

The results from the X-ray diffraction (XRD) analysis of both the coal and shale samples, which was conducted across varying depths, are summarised in Table 1. The samples predominantly contain quartz, CM component, and muscovite as major minerals, with trace amounts of feldspar, microcline, and siderite present in some samples. Kaolinite is the dominant CM component, while illite is also identified in the samples. Coal samples have a significantly higher CM content (ranging from 49 % to 86 %) compared to shale samples (ranging from 39 % to 59 %). Among the coal samples, KB 3 exhibits the highest CM content at 86 %, while KB 7 has the lowest at 49 %. In shale samples, SH 3 has the maximum CM content, while SH 4 shows the minimum.

The OM characteristics were determined using Rock-Eval pyrolysis, as shown in Table 2. The TOC values for coal samples range from 18.63 % to 55.84 %, while for shale samples, the TOC ranges from 0.73 % to 9.14 %. Based on the results, KB 2, KB 3, and KB 8 are classified as 'peak

Table 2
Thermal characteristics of the organic matter of studied coal and shales.

Sample ID	Depth (m)	S1 (mg/g)	S2 (mg/g)	T_{max} (°C)	PC (%)	RC (%)	TOC (%)	HI (mg HC/g TOC)	OI (mg CO_2/g TOC)
KB 1	170	0.27	43.16	422	4.08	33.63	37.71	114	13
KB 2	194	0.45	85.1	423	8.17	47.55	55.72	153	18
KB 3	255	2.09	211.12	421	18.27	37.32	55.59	380	10
KB 4	285	1.4	169.94	424	14.73	34.09	48.82	348	10
KB 5	306	1.31	146.93	419	12.7	29.31	42.01	350	9
KB 6	364	0.13	24.71	432	2.3	16.33	18.63	133	11
KB 7	534	0.22	68.03	427	5.86	22.98	28.84	236	5
KB 8	711	1.29	37.9	425	3.66	52.18	55.84	68	6
SH 1	182	0.11	2.36	427	0.31	3.45	3.76	63	69
SH 2	289	0.21	4.07	431	0.41	3.44	3.85	106	18
SH 3	329	0.22	3.52	429	0.36	3.31	3.67	96	17
SH 4	490	0.31	10.68	431	1	8.14	9.14	117	10
SH 5	582	0.08	0.3	357	0.05	0.68	0.73	41	42

mature'; KB 1, KB 4, and KB 5 as 'intermediate mature'; and KB 6 and KB 7 are carbonaceous shales with 'early maturity.' Shale samples, SH 1, SH 2, SH 3, SH 4 and SH 5, are categorised as 'immature' (see Table 2). The HI values vary between 41 and 380, while the OI ranges from 5 to 69, indicating the HC potential of the OM within the rock samples (as seen in Fig. 3). Fig. 3 shows that the samples predominantly lie between Type II and Type III OM, signifying a mixture of oil- and gas-prone kerogen types.

3.2. Nanoscale pore mapping

High-resolution imaging methods are employed to characterize coal and shale samples. The techniques provide insights into pore morphology and structure, including shapes and sizes. Fluid-invasive methods such as LPGA and MICP yield quantitative data on pore volume and surface area, while imaging techniques offer qualitative insights into pore structures. Coal and shale are complex, heterogeneous materials of various minerals and OM. Notably, coal majorly comprises organic pores, while shale exhibits distinct pore behaviours, including organic pores (which cluster in OM regions), intraparticle pores (pores enclosed within a mineral particle), and interparticle pores (pores which form in the space between two mineral particles) [67–72]. Organic pores in shale are crucial for storing SG, with gas adsorption primarily influenced by the OM present. In this context, the pore structure of shale formations is more complex than that of coal, as shales contain both organic and inorganic pores. However, the higher heterogeneity of shale makes it challenging to study the characteristics of both organic and inorganic pores [70]. Therefore, comparing the pore structures of coal and shale will enhance our understanding of organic pores in shale formations. Different mineral types exhibit distinct sizes, shapes, and rough aperture areas. The SEM observations in Fig. 4 reveal an abundance of nano- to micron-scale pores in the samples. The pores are often enclosed within OM, CM, and microfractures. The OM pores are round and can be isolated, interconnected, or intra-connected, while CM pores are associated with clay-OM aggregates, clay platelets, and clay clusters. The OM shows a substantial role in gas production and storage in the subsurface. The SEM studies show limitations in accurately quantifying pores that are smaller than 5 nm. However, significant attention is given

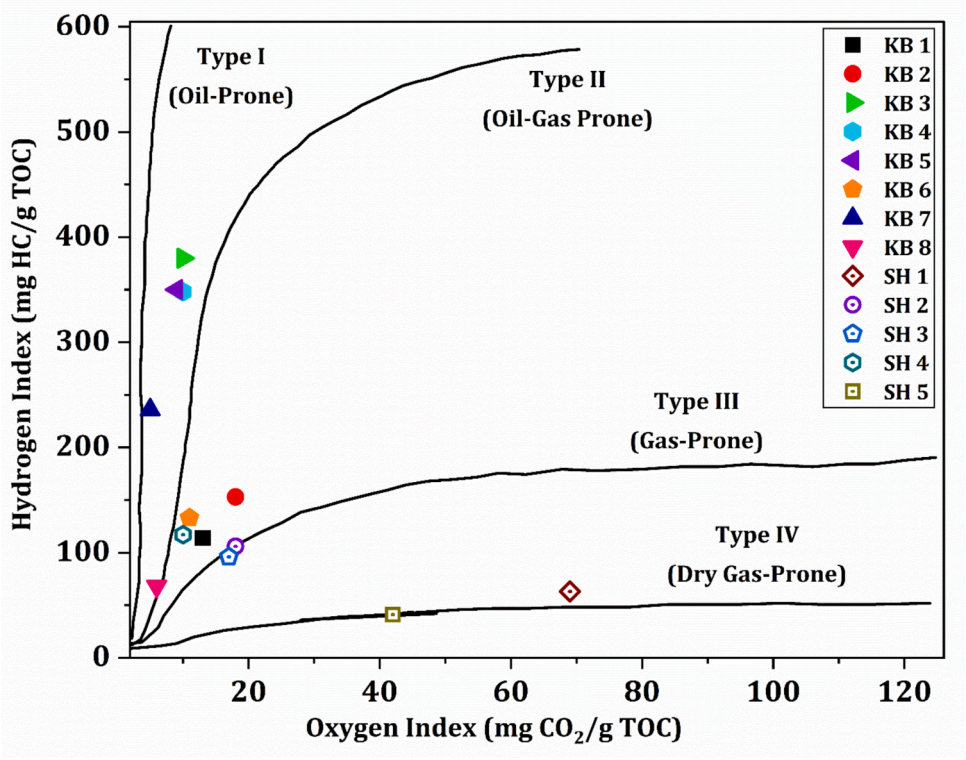

Fig. 3. Modified van Krevelen plot for the studied samples, determined using Rock-eval pyrolysis.

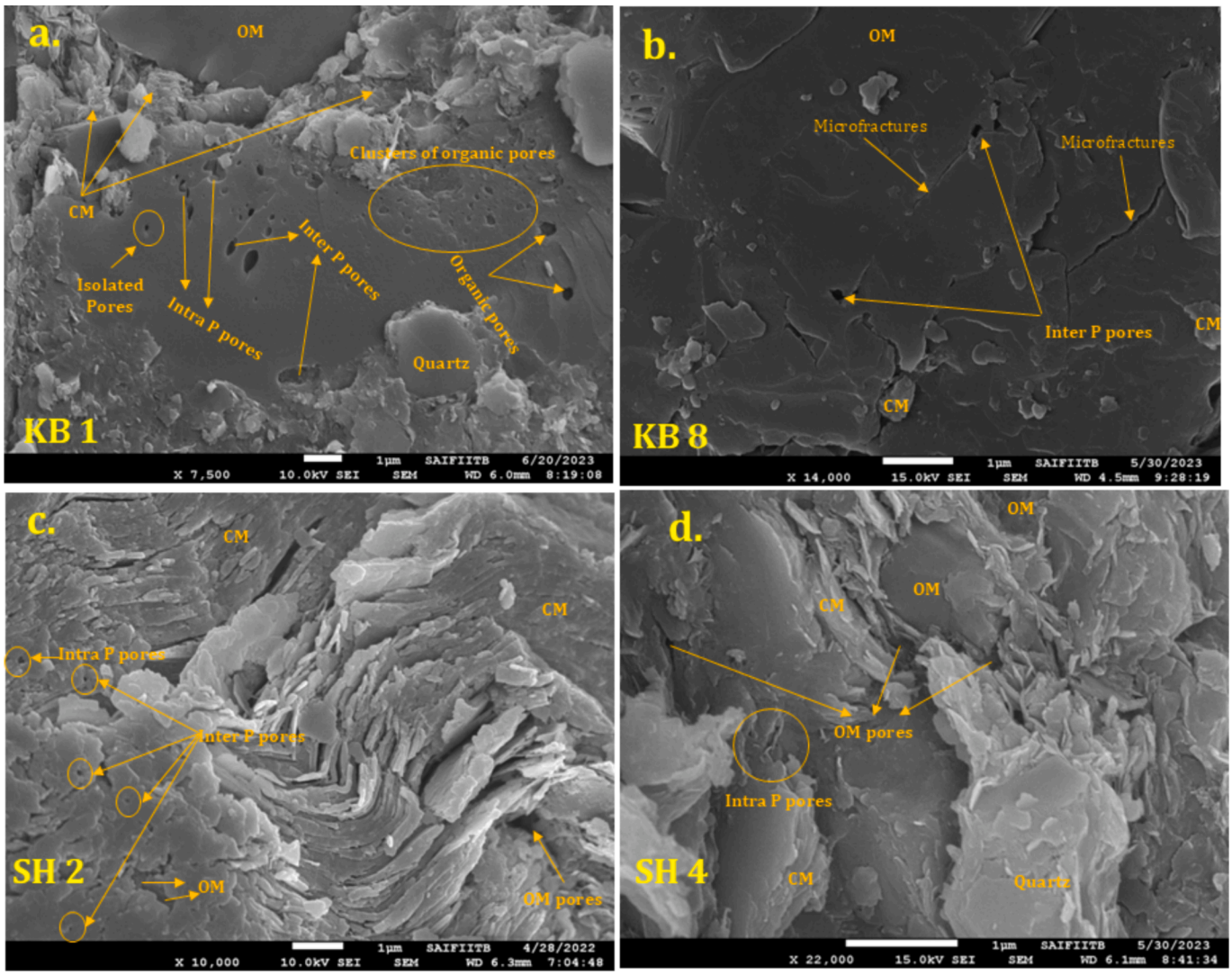

Fig. 4. (a, b) Field-Emission SEM (FE-SEM) images for coal (KB) and (c, d) shale (SH) samples, showing inter P pores, intra P pores, organic pores, and microfractures.

to pore distribution in this size range because the majority of gas storage occurs in micropores and mesopores [73]. In Fig. 4a, clusters of larger pores are observed, while the accumulation of nanopores indicates a higher gas-adsorption capacity in coal, which is primarily influenced by OM. The figure also illustrates the isolated pores, intraP pores, interP pores, and organic pores present in the sample. Fig. 4b shows a section with a high OM content and traces of quartz and CM. Sample KB 8 exhibits interparticle pores and microfractures, facilitating gas transport from micropores to mesopores and macropores, thereby maximizing gas adsorption. Fig. 4c indicates the presence of clay minerals (kaolinite). The morphological examination reveals that the stacking of numerous platelets forms a "booklet-like structure," with sizes ranging up to tens of micrometers, prominently exposing the edge surfaces [72]. Fig. 4d illustrates the morphology of quartz in proximity to organic matter. The figure highlights OM pores within the sample, which can contribute to gas adsorption and facilitate CO_2 storage in subsurface formations. The SEM images of other samples are provided in the supplementary file, Fig. S1.

3.3. Sub-micron pore structure analysis

3.3.1. Low-pressure gas adsorption profiles

Fig. 5a and 5c show the N_2 adsorption–desorption isotherm curves for coal and shale samples, respectively. In the study, the isotherm is classified as Type IV with H3 hysteresis, indicating a process where initially, the N_2 gas molecule occupies micro- and monolayer voids, followed by multilayer formations and capillary condensation within porous samples through the mechanism of physisorption. The N_2 adsorption curve represents this, while the emptying of pores (capillary evaporation, multilayer and monolayer formation, and micropore filling) occurs in the reverse order and is termed the N_2 gas desorption. Fig. 5a and 5c reveal a sudden drop in the desorption curve around (P/Po) ~ 0.45–0.60, which is attributed to rapid emptying and cavitation in the pores; this is known as the tensile strength effect (TSE) [74]. Consequently, the desorption curve is not used for characterising pore structures. The adsorption capacity in coal samples ranges from 5.67 – 30.447 cc/g. In the study, sample SH 3 shows unexpectedly high mesoporosity, ranging from 26.16 to 37.49 cc/g at (P/Po) > 0.95. This deviation in SH 3 may be attributed to its higher kaolinite content. Fig. 5b and 5d present the CO_2 adsorption isotherms for coal and shale samples, respectively. The isotherms are classified as Type I, indicating the filling of micropores at active sites across all samples. The adsorption capacity in the coal samples varies from 4.74 – 16.91 cc/g, while the adsorption capacity in the shale samples varies from 1.79 – 5.94 cc/g. These observations suggest that samples SH 5, SH 3, and KB 7 possess higher sorption potential in mesopores, whereas SH 4 and KB 2 exhibit greater

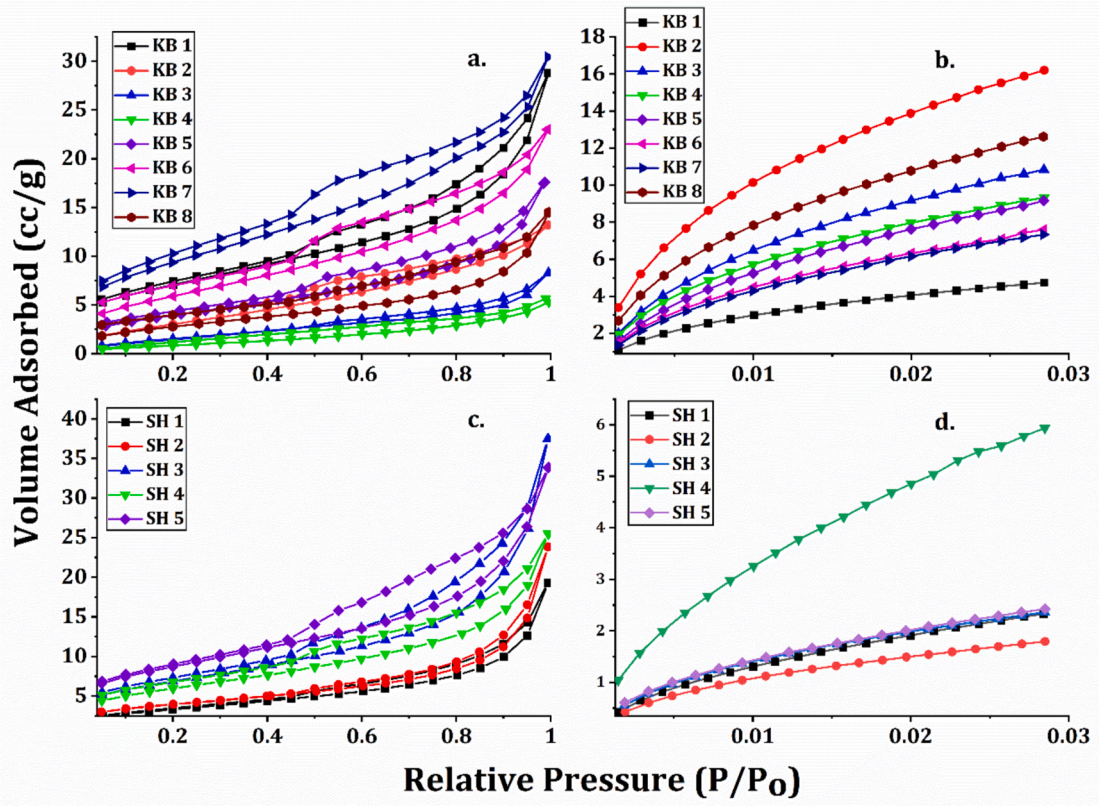

Fig. 5. Adsorption Isotherm curves determined from **(a, c)** N_2 gas at 77 K and **(b, d)** CO_2 gas at 273 K. Fig. 5 **(a, b)** represents data from coal samples, while Fig. 5 **(c, d)** represents data from shale samples collected from the Korba Basin.

sorption potential in micropores in shale and coal samples, respectively, as further displayed in Fig. 5.

3.3.2. *Mercury intrusion-driven pore analysis*

Fig. 6 displays the mercury intrusion and extrusion (MIE) curves, which were obtained from the MICP method, for both (a) coal and (b) shale samples. The differences in pore characteristics significantly influence the MIE curves for both coal and shale samples. The curves for the coal samples shown in Fig. 6a differ markedly from those of the shale samples in Fig. 6b, particularly at higher pressures or within the lower pore size range (micro- and mesopore segments). In this segment, there is a notable gap between the MIE curves for both coal and shale, indicating that the pores are predominantly open. In the segment above 100 nm, the mercury extrusion curves for both coal and shale formations show a significant variance from the mercury intrusion curves. Among the coal and shale samples, KB 3 and SH 2 shows the maximum mercury intrusion at pressures of up to 60,000 psi, reflecting the peak cumulative PV among the samples. Notably, the mercury intrusion volume is greater

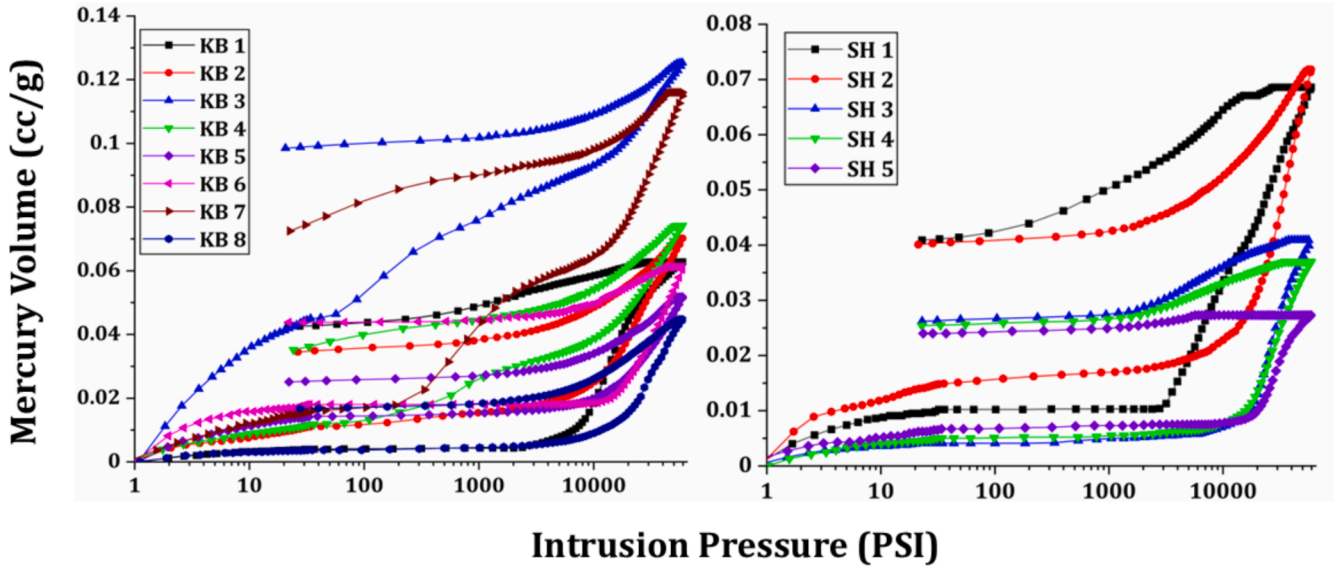

Fig. 6. MIE curves, determined by MICP method for a) coal (left) and b) shale samples (right).

in coal samples (0.122 cc/g) than in shale samples (0.0705 cc/g).

3.3.3. Sub-micron structural profiling

Figs. 7a. and b. present the plots of intensity scattering vector I(Q) versus scattering wave vector (Q) profiles for coal and shale samples, respectively. The scattering profiles indicate a similarity across all coal and shale samples, which suggests low heterogeneity that is attributed to the uniformity of the pulverized samples. The advanced small angle scattering (SAS) technique can quantify a wide range of pore sizes, from 1 nm to 200 nm. In this study, the Q values range from 0.005 to 0.1 ($Å^{-1}$). This non-invasive method enables the assessment of both inaccessible and accessible pores in the samples. The intensity scattering profile for shale is higher than that of coal samples, which can be attributed to the higher mineral content, specifically quartz, and muscovite.

3.4. Nanoscale structure analysis

3.4.1. Multiscale pore analysis through gas-adsorption method.

Mesopore SA calculated using the BET equation for coal samples varies from 3.73 to 33.84 m^2/g, while for shale samples it ranges from 12.03 to 30.79 m^2/g. The micropore SA determined using the DR method varies from 48.4 to 173.02 m^2/g for coal samples, and from 18.24 to 67.54 m^2/g for shale samples, as detailed in Table A1 of the supplementary files. Subsequently, the mesopore volume for coal and shale samples varies from 0.007 to 0.041 cc/g and 0.023 to 0.046 cc/g, respectively. In contrast, the micropore volumes range from 0.026 to 0.074 cc/g for coal and 0.01 to 0.078 cc/g for shale. Notably, the total PV for coal and shale varies from 0.058 to 0.097 cc/g and 0.038 to 0.11 cc/g, respectively, as detailed in Table A2 of the supplementary files. The average PW for the coal samples ranges from 5.57 to 8.82 nm, while for the shale samples, it varies from 6.8 to 10.81 nm. This suggests that samples with smaller PW occupy (or adsorb) a higher volume of gas within their pore structure.

3.4.2. Meso- and macroscale pore structure analysis using the SAXS method

Fig. 8 shows the SA and PV for the coal and shale samples, as determined by SAXS methods. The tables illustrate the distribution of the macrospores, mesopores, and total pore characteristics within the samples. The total pore SA for the coal samples ranges from 9.27 m^2/g to 48.61 m^2/g, while for the shale samples, it varies from 17.46 m^2/g to 43.81 m^2/g. The total PV for the coal samples ranges from 0.021 cc/g to 0.099 cc/g, whereas for the shale samples, it ranges from 0.054 cc/g to 0.113 cc/g. Notably, the samples exhibit a higher proportion of mesopores than macropores, indicating that the SAXS method is particularly effective for characterising pore structures in the mesopore size range. Samples KB 4 and SH 2 show the least surface area and pore volume than other coal and shale samples, respectively. This discrepancy is attributed due to its high TOC and a greater abundance of micropores.

3.4.3. Comprehensive nano-to-micron scale pore-network assessment using MICP

According to Fig. 8, pore attributes, including SA and PV of coal and shale samples, were determined using high-pressure MICP (HP-MICP). For the sake of an even comparison, we assumed the total surface area (surface area from LPGA+MICP+SAXS) normalized to 100 for each individual sample. Same treatment was done for pore volumes as well. The normalised SA for the coal samples ranges from 9.99 to 18.193 m^2/g, which is lower than that for the shale samples, which ranges from 7.099 to 38.87 m^2/g. Subsequently, the figure provides the normalised total PV for both coal and shale samples. The normalised PV for coal samples ranges from 0.225 to 0.553 cc/g, which is greater than the normalised PV for shale samples, which ranges from 0.089 to 0.439 cc/g. The higher pore attributes observed in coal samples may be attributed to the higher order of natural fractures or cleats, which cannot be determined using LPGA method.

3.5. Comprehensive nanoscale pore size distribution

Fig. 9 provides a broad overview of the PSD in coal and shale samples ($CO_2 - N_2$). Gas adsorption isotherm and MICP intrusion data have been combined to elucidate the size distribution of micropores, mesopore, and macropore properties. These measurements were obtained using fluid-invasion techniques, specifically the LPGA (0.3–36 nm) and MICP (3.6–100,000 nm) methods. Fig. 9a displays differential PV for coal samples, in which the peaks are notably higher in the micropore region but decrease as the pore diameter increases. Samples with high TOC display elevated peaks at the lower size ranges, while those with significant mineral contents show increased peaks at larger ranges (> 2 nm). The PV in the mesopore region decreases and diminishes in the macropore region (with the exception of KB 3, KB 4, and KB 7), revealing the dominance of OM. This suggests a good correlation between the micropore volume and the OM content. In contrast, coal samples demonstrate a significant PV peak in pore sizes greater than 100 nm, whereas shale samples do not exhibit any peaks in this size range. The peaks observed in coal samples KB 3, KB 4, and KB 7 at sizes exceeding 100 nm are likely attributed to the microfractures present in the samples, as evident from the SEM images. Fig. 9b shows the differential PV for shale samples, where the peaks are more pronounced in the mesopore region and less so in the micropore region (with the exception of SH 4), while the macropore region exhibits minimal volume.

Fig. 10a and b present the PSD calculated from the SAXS scattering profiles for both coal and shale samples, respectively. The PSD is characterised using the polydisperse spherical model (PDSP) Eqs. (4), (5) and (6) via the MATSAS script, which is a MATLAB module. The SAXS raw data files include both the intensity I(Q) and the Q data, along with the calculated SLD and the mean density values for the samples. For the void space (pore), the SLD values are assumed to be zero.

The scattering intensity vector, I(Q), for an ideal PDSP scatter, is represented as follows:

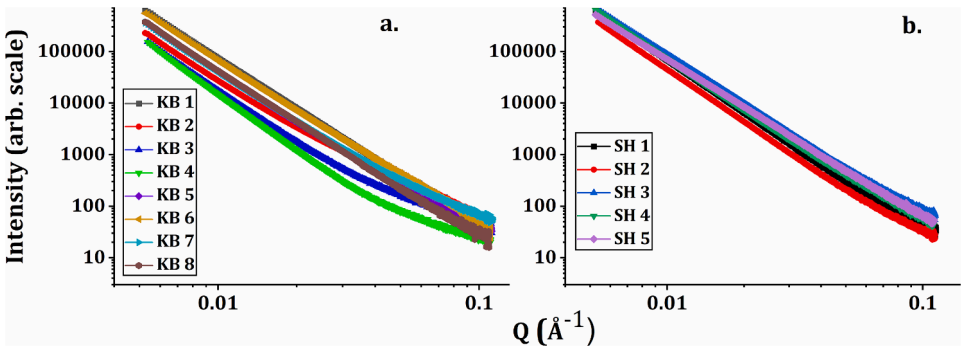

Fig. 7. Intensity scattering profile for a) coal samples and b) shale samples determined by SAXS method.

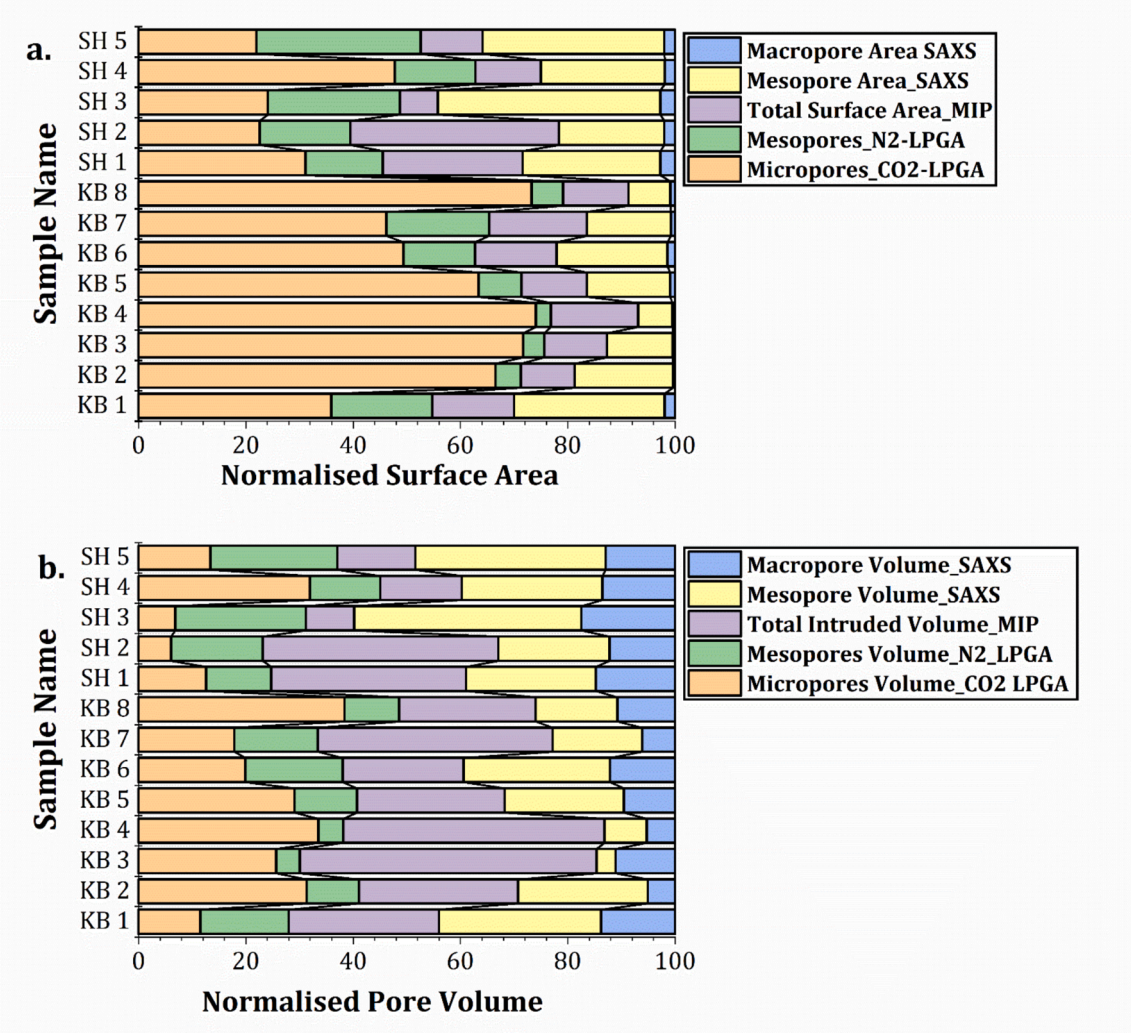

Fig. 8. Integrated (micro-, meso-, macro- and total) a. Normalised SA and b. Normalised PV of coal and shale samples.

$$I(Q) = \sum_n C_n \int_{R_{min}}^{R_{max}} r^6 P(Q,r) f(r, D_n, R_{max}, R_{min}) dr \tag{4}$$

C_n is independent of Q.

$$P(Q,r) = \left[3\frac{\sin(Q,r) - Qr\cos(Q,r)}{Q^3 r^3}\right]^2 \tag{5}$$

where, f (r, D_n, R_{max}, R_{min}) indicates the power-law PSD for the n^{th} order.

$$f(r, D_{-n}, R_{-max}, R_{min}) = \frac{\left[r^{-(1+D_n)}\right]}{\left[\frac{R_{min}^{(-Dn)} - R_{min}^{(-Dn)}}{D_n}\right]} \tag{6}$$

In Fig. 10a, the observation suggests that KB 2 has an abundance of micropores, whereas KB 1 contains a large proportion of mesopores. The SAXS results align closely with those obtained from the LPGA analysis. Notably, the PSD increases again around 20 nm and becomes significant in the pore size range of approximately 60 nm. The PSD for shale samples peaks at around 4 nm (Fig. 10b), with SH 3 displaying the maximum PSD value and KB 4 the minimum among the samples, as seen in Fig. 10a and 10b. There is a marked increase in PSD in the pore size range of approximately 15 nm to 90 nm. The PSD curves for both coal and shale samples exhibit a similar trend; however, the differential PV for the shale is higher than that for the coal samples.

3.6. Measure of structural complexity

The fractal dimension (D_f) measures the irregularity of pore surfaces in samples, reflecting the roughness factor and its influence on the adsorption potential. Based on N_2 gas-adsorption isotherms, the Frenkel–Halsey–Hill (FHH) model is employed to calculate the fractal behaviour in porous media. In addition Df for SAXS and MICP method is determined using Power-law and Menger Sponge equations, respectively as mentioned in Table 3. The fractal dimension (D_f), which is calculated from the LPGA is directly proportional to the number of active surface sites available in the adsorbate. The plot of $\ln(V_{adsorbed})$ versus $[\ln(\ln(P/P_0))]$ at different (P/P_0) regimes provides the fractal dimension, $(D_f)_{LPGA}$, as explained in [42]. The mean fractal dimension, $(D_f)_{mean}$, is determined using the average values of D_{N1} and D_{N2}, which facilitates the correlation of $(D_f)_{LPGA}$ with other methods such as $(D_f)_{MICP}$ and $(D_f)_{SAXS}$. The difference between the isotherms at the two (P/P_0) regimes reflects the variations in the adsorption properties. In the low-pressure regime ($0.01 < P/P_0 < 0.5$), van der Waals forces primarily govern the interactions between the adsorbate and the adsorbent due to low surface tension. Conversely, in the high-pressure regime ($0.5 < P/P_0 < 0.99$), surface tension becomes more significant, and capillary condensation plays a crucial role in determining fractal characteristics. Table 4 illustrates the values of D_{N1} and D_{N2} for coal and shale samples, which shows similarity to [75,76]. The coal samples exhibit lower $(D_f)_{LPGA}$ values, ranging from 2.14 to 2.54, while the shale samples show

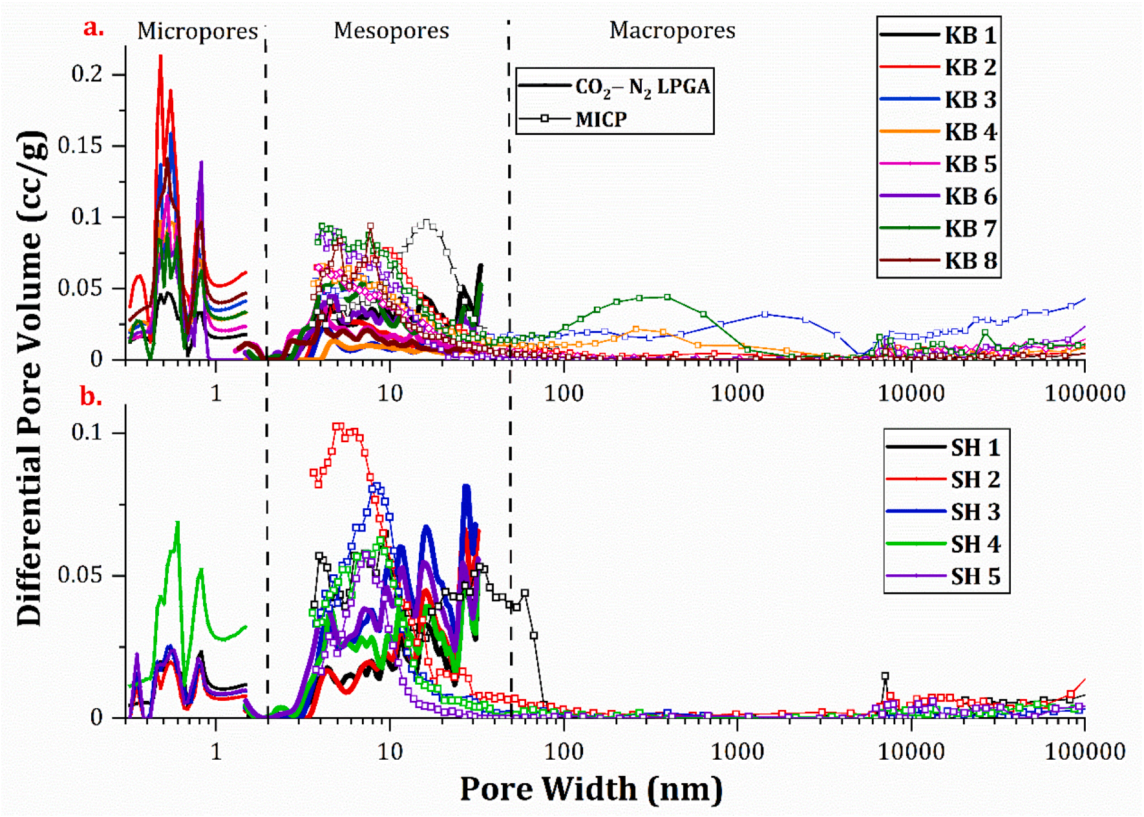

Fig. 9. Integrated PSD calculation of a) coal and b) shale samples, calculated by combining the LPGA and MICP methods.

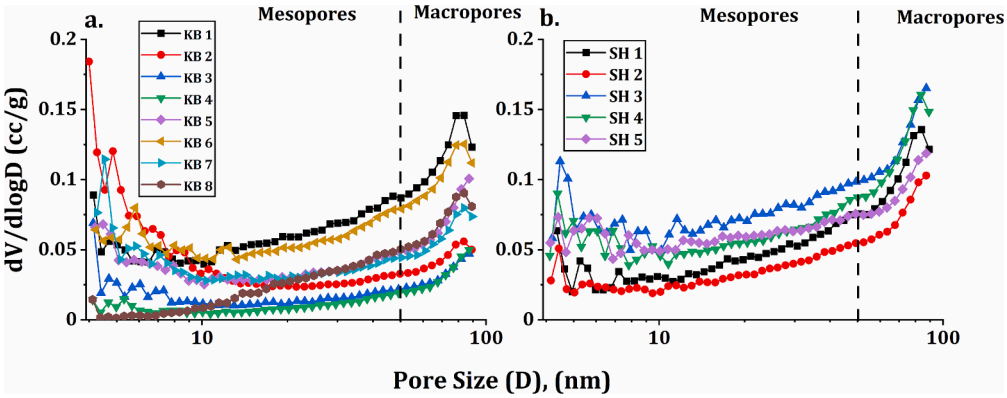

Fig. 10. PSD calculation of a) coal samples and b) shale samples determined by the SAXS method.

$(D_f)_{LPGA}$ values between 2.51 and 2.58 at a low relative pressure region. At higher rel. pressure range. The coal samples reveal $(D_f)_{LPGA}$ values ranging from 2.26 to 2.52, while the shale samples show $(Df)_{LPGA}$ values between 2.51 and 2.58, a higher rel. pressured range. The plots for the fractal dimension calculated using the LPGA method are shown in the supplementary file, figure S2.

The fractal dimension $(D_f)_{SAXS}$ for both coal and shale samples is determined using the SAXS method. The coal samples exhibit higher $(D_f)_{SAXS}$ values, ranging from 2.39 to 3.00, while the shale samples show $(D_f)_{SAXS}$ values between 2.72 and 2.82. In contrast, the pore size range for the LPGA method is limited to 0.4–36 nm, whereas the SAXS method encompasses a broader range of 4–100 nm. This difference explains why $(D_f)_{SAXS}$ are greater than $(D_f)_{LPGA}$; the SAXS method shows significant meso- and microporosity characteristics when compared to the LPGA method, as shown in Table 4. In this research, the fractal dimension $(D_f)_{MICP}$ is analysed using the mercury intrusion curve and the Merger Sponge (M−S) model [65,77] to assess surface roughness in both coal and shale samples at the meso- and macropore scales. These sedimentary rocks are inherently heterogeneous, which impacts fluid-flow kinetics and gas transport in gas reservoirs. Feng et al. [65] demonstrated that the M−S model is widely used to provide fractal characteristics in porous media, including coal and shale. Initially, mercury enters the penetrometer and begins to fill the interparticle spaces between solid sample blocks. The effect of these interparticle spaces is often neglected because the pore sizes at this pressure range exceed 100 μm. In this study, the fractal analysis is categorised into three stages based on the findings of Feng et al. [65]: Stage A ($P_{Hg} < 25$ MPa, $d > 50$ nm), Stage B (25 MPa $< P_{Hg} <$ 137.7, $d < 50$ nm) and Stage C ($P_{Hg} > 137.7$). In Stage A, mercury fills the PV of accessible pores, illustrating the pore heterogeneity in the samples, which allows for determining the fractal dimension (D_{M1}) for this stage. In Stage B, the pore matrix experiences compression due to high pressures, resulting in a reduction of the matrix

Table 3
Representation of fractal dimension models of various methods such as LPGA, SAXS and MICP.

Method	Fractal Dimension (D_F)	References
Frenkel – Halsey – Hill (FHH)	D_N in the capillary condensation regime is given as equation below $\ln(\frac{V}{Vm}) = C + M \ln[\ln(\frac{P}{Po})]$ At region $(0.01 < (P/P_o) < 0.5)$, $M_1 = (D_{N1} - 3)$ At region $(0.5 < (P/P_o) < 0.99)$, $M_2 = \frac{(D_{N2} - 3)}{3}$ Mean Fractal Dimension, Mean $D_N = [\frac{DN1 + DN2}{2}]$	[16,61,62]
Power-law equation	The surface fractal dimension (Ds) can be determined using the slope (S) of the log–log plot of I(Q) vs Q data, which follows a power-law equation, $I(Q) \propto Q_S^{6-D}$ $D_s = 6 - S$	[30,63,64]
Menger Sponge	At a specific pressure, the injection volume ($dV_{P(r)}$) corresponds to the total PV at a given radius (r). $dV(r) = dV_{P(r)}$ $\frac{dV_{P(r)}}{dP(r)} \propto \left[\frac{r}{P(r)}\right] * r^{2-D} D = 4 + \frac{\log\left(\frac{dV_P}{dP(r)}\right)}{\log(P(r))}$ A plot between $\frac{dV_{P(r)}}{dP(r)}$ and dP (r) or $\log \frac{dV_{P(r)}}{dP(r)}$ *and* log dP (r) can be drawn. This plot will yield a slope (K), allowing to determine the pore fractal dimension $(D_f)_{MICP}$ using MICP method.	[65,66]

PV. The PV measured during this stage is often greater than the actual PV, leading to inaccuracies in assessing pore characteristics. The fractal dimension (D_{M2}) calculated from Stage B is typically greater than 3 or 4, rendering these values non-physical. Consequently, (D_{M2}) increases with the degree of compression. Similar findings have been reported by [78]. In Stage C, the pore characteristics of the samples change or distort under the influence of high pressure and matrix compression, leading to the generation of new microfractures or the connection of closed pores. Since multiple effects influence the pore dimensions in this stage, the fractal dimension (D_{M3}) becomes invalid. Several Authors [79,80] have observed that the MICP method tends to overestimate the PV due to the compressibility of both coal and shale. According to Table 4, the fractal dimension data obtained from Stage A can be considered valid. However, the fractal dimensions obtained from Stages B and C are uncertain for pore characterisation below 50 nm. Therefore, the HP-MICP method proves effective for macropore characterisation but is ineffective for pores smaller than 50 nm. The plots for the fractal dimension calculated using the MICP method are shown in the supplementary file, figure S3.

It has been experimental demonstrated that the mercury injection at a higher pressure can result in coal matrix compression [78,79,81]. In addition, the authors have derived a model to determine the corrected pore volume from the coal matrix at higher injection pressure. The coal matrix compressibility, can be defined as Eq. (7),

$$\beta = -\frac{1}{V_o}\left(\frac{dV_o}{dP}\right) \tag{7}$$

The measured mercury volume is the sum of the pore filling volume determine using LPGA method and the compression-induced matrix deformation determined using MICP Eqs. (8) and (9).

$$\Delta V_{Hg} = \Delta V_{pore} + \Delta V_o \tag{8}$$

$$\frac{\Delta V_{Hg}}{\Delta P} = \frac{\Delta V_{pore}}{\Delta P} + \frac{\Delta V_o}{\Delta P} \tag{9}$$

Combining Eqs. (7), (8) and (9), the compressibility can be calculated as Eq. (10)

$$\beta = \left[-\frac{1}{\Delta V_o}\left(\frac{\sum_{100MPa}^{210MPa}\Delta V_{Hg}}{\Delta P} - \frac{\sum_{6nm}^{12.2nm}\Delta V_{Pore}}{\Delta P}\right)\right] \tag{10}$$

In addition to this, Li et al. [78] illustrated that the matrix compression effect is insignificant at pressures (<20 MPa). At pressures (>20 MPa), as compressibility increases, the inconsistency between the raw mercury intrusion data and corrected intruded mercury volume also increases. One of the limitations of the corrected pore model is the assumption that the pores are spherical, which does not correctly represent the sample used for analysis. Therefore, this model cannot be applied for the interparticle pore effect correction of MIP data of coal samples.

The corrected pore volume from MICP data can be determined by subtracting the induced compression from the observed intrusion volume Eqs. (11) and (12).

$$\Delta V_{pore}(P_i) = \Delta V_{Hg}(P_i) - \Delta V_o(P_i) \tag{11}$$

$$= \Delta V_{Hg}(P_i) - \Delta V_{Hg}(P_{i-1}) - CV_{CV}(P_{i-1})(P_i - P_{i-1}) \tag{12}$$

where, $V_{CV}(P_{i-1})$ is the compressible volume of sample matrix at pressure (P_{i-1}), (cc/g).

Since, the skeleton density for the coal and shale samples were not recorded during measurement, the skeleton density for coal samples is assumed to be around 1.4 (g/cc) [78], while for the shale samples it is

Table 4
Fractal dimension of coal and shale samples.

Sample ID	LPGA			MICP			SAXS	$(D_F)_{SAXS}$ – (Mean D_N)
	$D_{N1} = [0.01 < (P/P_o) < 0.5]$	$D_{N2} = [0.5 < (P/P_o) < 0.99]$	Mean $D_N = [\frac{DN1 + DN2}{2}]$	D_{M1} at (< 25 MPa)	D_{M2} at (25 MPa < P < 137.7 MPa)	D_{M3} at (P > 137.7 MPa)	$(D_F)_{SAXS}$	
KB 1	2.54	2.37	2.46	3.16	4.55	2.3	2.74	0.28
KB 2	2.27	2.49	2.38	2.96	4.28	2.82	2.99	0.62
KB 3	2.14	2.37	2.26	2.94	3.64	2.97	2.70	0.44
KB 4	2.14	2.37	2.26	3.12	3.92	3.23	2.39	0.13
KB 5	2.42	2.46	2.44	2.75	4.38	3.57	2.75	0.31
KB 6	2.45	2.46	2.46	3.07	4.21	3.25	2.76	0.30
KB 7	2.52	2.52	2.52	3.18	4.06	3.2	2.82	0.30
KB 8	2.42	2.34	2.38	2.94	4.29	3.04	2.71	0.33
SH 1	2.51	2.16	2.34	3.13	2.77	2.76	2.61	0.27
SH 2	2.58	2.69	2.64	2.83	4.22	3.45	2.61	−0.03
SH 3	2.56	2.01	2.29	2.56	4.57	2.72	2.82	0.53
SH 4	2.54	2.34	2.44	3.09	3.57	3.94	2.71	0.27
SH 5	2.56	2.07	2.32	2.74	5.89	2.14	2.89	0.57

2.4 (g/cc) [46].

The compressibility values and corrected pore volume for the coal (KB) and shale (SH) samples are listed in Table 5. The comparison of results for coal and shale samples shows the compressibility varies from 1.5 x 10^{-10} to 2.8 x 10^{-10} (Pa^{-1}) and 2.07 x 10^{-10} to 4.1 x 10^{-10} (Pa^{-1}), respectively, which is consistent with the results from Li et al, [78] and Feng et al. [79]. In addition, the corrected pore volume for coal and shale varies as 0.034 – 0.068 (cc/g) and 0.032 – 0.053 (cc/g), respectively. Furthermore, the compression-induced error (%) ranges from 26.706 to 92.646 and 32.92 – 94.521 for coal and shales respectively.

4. Discussion

4.1. Degree of pore connectivity

The degree of pore connectivity (DPC) in coal and shale refers to the extent to which the pores are distributed and interconnected, which is essential for understanding fluid flow and gas transport in subsurface formations. The pore connectivity depends on how these pores develop and connect to the existing network. Chandra et al. [59] also identified the variations in the DPC in shale samples. It ranges between 0 and 1, indicating 0 for isolated (no connected) pores, while 1 for a fully connected pore system.

$$\textbf{\textit{Degree of pore connectivity}} = \left(\frac{Accessible\ pore\ volume}{Total\ pore\ volume}\right) = \left(\frac{Mesopore\ volume\ from\ LPGA}{Mesopore\ volume\ from\ SAXS}\right) \quad (13)$$

This study discusses the DPC in coal and shale, which is determined by the ratio of accessible PV calculated using the LPGA method to the total (inaccessible + accessible) PV calculated using the SAXS method. The higher pore connectivity ratio indicates a well-connected network, while a lower ratio suggests isolated, unconnected pores that remain inaccessible.

The mesopore volume in the LPGA method was determined using the Kelvin equation, which assumes cylindrical pore shapes and is primarily applicable to mesopores and macropores. Several studies have shown that the Kelvin equation does not account for the effects of pore wall–fluid interactions and the associated inhomogeneity of the pore fluid. It has been shown that the Kelvin equation underestimates pore size and may not be reliable for pores smaller than 7.5 nm [80,82]. Thommes [83] reported that the corrected Kelvin equation underestimates pore size by approximately 25 % for pores < 10 nm. The Kelvin model calculates pore volume based on a range of pore size from 2 – 400 nm. Here we are concerned about mesopore connectivity, hence we are comparing mesopore volume calculated from DFT based on LPGA data and mesopore volume from SAXS data using PDSP model. The advantage of the DFT method over the classical approach is its applicability to both capillary condensation and micropore filling. This adjustment has enhanced the comparability of LPGA and SAXS pore volumes by considering a similar pore size range when calculating the degree of pore connectivity.

Table 6 shows the DPC values for coal and shale samples, ranging from 0.40 to 0.93 and 0.50 to 0.82, respectively. The observation states that the pore structure in coal predominantly involves a suitable network of micropores, which dominates gas adsorption, while mesopores and macropores act as passages connecting these micropores. In light of this, the shale formations display a more complex pore structure composed of micro- and mesopores. Zhao et al. [84] shows that the TOC and mineral composition in shale samples are critical factors influencing the DPC. In coal samples, OM may swell during gas adsorption, reducing pore connectivity. Similarly, mineral compositions can hinder the path, further decreasing connectivity. Sun et al. [85] revealed that brittle minerals, such as quartz, feldspar, muscovite, and microcline, can reduce pore connectivity by isolating the gas system. Shale pore connectivity is often limited due to the predominance of isolated nanopores. Higher clay content typically reduces connectivity because clay tends to form poorly connected pore systems, although fractures within clay layers can enhance pathways. Both natural and induced fractures

Table 5
Compressibility, Corrected Pore Volume and related parameter calculation for coal (KB) and shale (SH) samples.

Sample Name	Slope	Intercept	R^2	Skeleton density (g/cc)	Compressibility (Pa^{-1})	Raw Pore Volume (cc/g)	Corrected Pore Volume (cc/g)	Compressed −Induced Volume[a] (cc/g)	Compression −Induced Error[b] (%)	Calculation Error[c] (%)
KB1	1.14E-06	0.020	0.97	1.4	2.28E-10	0.094	0.068	0.026	38.012	27.543
KB2	1.40E-06	0.010	0.99	1.4	2.8E-10	0.071	0.056	0.015	26.706	21.077
KB3	8.64E-07	0.084	0.99	1.4	1.74E-10	0.057	0.041	0.016	38.091	27.584
KB4	9.04E-07	0.030	0.99	1.4	1.82E-10	0.057	0.045	0.013	28.294	22.054
KB5	7.54E-07	0.012	0.99	1.4	1.5E-10	0.048	0.034	0.014	43.029	30.084
KB6	1.09E-06	0.004	0.99	1.4	2.17E-10	0.071	0.045	0.026	58.037	36.724
KB7	1.35E-06	0.049	0.99	1.4	2.69E-10	0.087	0.059	0.028	47.874	32.375
KB8	9.03E-07	−0.002	0.97	1.4	1.81E-10	0.070	0.036	0.034	92.647	48.091
SH1	1.01E-06	0.024	0.99	2.4	3.4E-10	0.058	0.044	0.014	32.920	24.767
SH2	1.15E-06	0.008	0.99	2.4	3.98E-10	0.093	0.053	0.040	75.994	43.180
SH3	1.19E-06	−0.010	0.99	2.4	4.1E-10	0.068	0.035	0.033	94.521	48.592
SH4	9.58E-07	−0.005	0.99	2.4	3.29E-10	0.056	0.033	0.023	68.445	40.634
SH5	6.13E-07	−0.002	0.98	2.4	2.07E-10	0.057	0.032	0.025	76.469	43.333

[a] **Compressed-Induced Volume:** [(Raw Pore Volume – Corrected Pore Volume)].
[b] **Compression-Induced Error**: [(Compression-Induced Volume)*100/(Corrected Pore Volume)], %.
[c] **Calculation Error:** [(Raw Pore Volume – Corrected Pore Volume)*100/(Raw Pore Volume)], %.

Table 6
Degree of Pore Connectivity for coal and shales.

Sample Details	LPGA	SAXS	Degree of Pore Connectivity (DPC)
	Mesopores Volume, (cc/g)	Mesopore Volume, (cc/g)	
KB 1	0.037	0.068	0.54
KB 2	0.023	0.057	0.40
KB 3	0.01	0.025	0.40
KB 4	0.007	0.012	0.58
KB 5	0.022	0.042	0.52
KB 6	0.042	0.063	0.67
KB 7	0.041	0.044	0.93
KB 8	0.018	0.027	0.67
SH 1	0.023	0.046	0.50
SH 2	0.028	0.034	0.82
SH 3	0.046	0.080	0.58
SH 4	0.032	0.064	0.50
SH 5	0.044	0.066	0.67

significantly improve shale connectivity [86–88]. Fig. 11a shows a positive correlation (37 %) between total SA, determined using the MIP method, and pore connectivity in shale samples, attributed to a large proportion of mesopores and macropores. Furthermore, Fig. 11b shows an excellent correlation (99 %) between micropore SA and the DPC in shale samples, likely due to the wide distribution of nanopores, in this case the outlier point is neglected and not included in calculating correlation. Fig. 11c shows positive correlation (46 %) between the fractal dimension from LPGA and DPC. The integrated approach to assessing pore connectivity provides valuable insights into the efficiency of coal and shale as potential reservoirs for gas production and storage, particularly for enhanced CBM and shale gas recovery.

4.2. *The effect of organic richness, mineral content, and depth on pore characteristics (micropores and mesopores) and surface roughness*

Fig. 12 (S1) shows a strong positive correlation is observed between mesopore SA and depth ($R^2 = 74$ %), while a strong negative correlation exists between average PW and depth ($R^2 = 83$ %). This suggests that with increasing depth, mesoporosity in shale samples increases while average PW decreases, enhancing the capacity for gas storage in deeper shale formations. Fig. 12 (S2) illustrates a negative correlation (91 %) between the total intruded volume calculated using MICP and depth for shale samples, in this case SH3 is neglected and not applied in plotting. It shows that the macroporosity in shale samples decreases with depth due to greater compaction in subsurface formations. This is attributed to clay structures accommodating larger pores, including mesopores. Fig. 12 (S3) indicates a negative correlation (34 %) between micropore SA and CM in shale samples. Fig. 12 (S3) shows a strong positive correlation (80 %) between the micropore SA and TOC (%) in shale samples. Fig. 12 (C1) shows the relationship between micropore SA, mesopore SA, and average PW with TOC (%) which shows a good fit with coefficients of determination (R^2) of 51 %, 57 %, and 37 %, respectively. [42] reported a similar (reversal) trend between mesopore SA and average PW, as observed in this study. The result is influenced by high TOC values in coal, which provides primary sites for gas storage. Fig. 12 (C2) illustrates a positive (41 %) and negative (52 %) correlation between micropore and mesopore volumes with TOC (%), reflecting similar trend to those in Fig. 12 (C1). In addition, coal is composed of organic matter and dominated with micropores than in mesopores. Fig. 12 (C3) shows the negative correlation (52 %) between the fractal dimension determined using the LPGA methods, respectively, with TOC (%) in shale samples. This indicates that TOC significantly influences surface roughness at smaller pore sizes (<50 nm), while its influence decreases as pore size increases (>50 nm). Fig. 12 (C4) demonstrates a negative correlation of (34 %) is evident between mesopore volume calculated using SAXS and TOC. This reflects the dominance of micropores in coal samples with

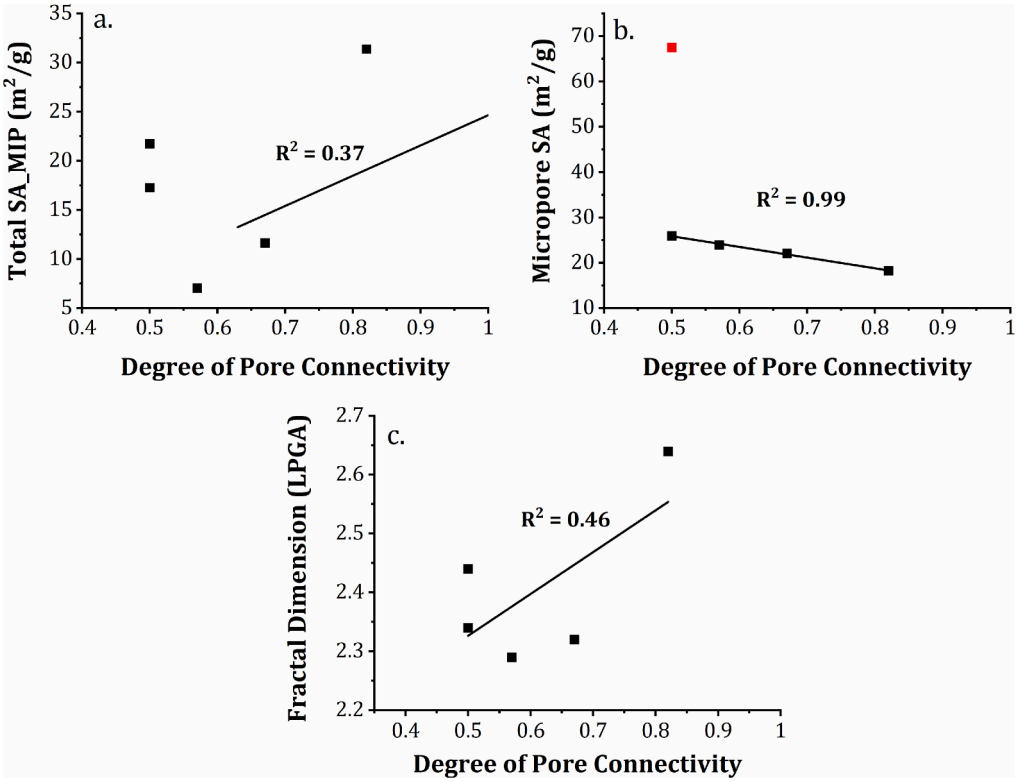

Fig. 11. Correlations between a. Total SA (MICP) (m^2/g) and degree of pore connectivity for shale samples; b. Micropore SA (m^2/g) and degree of pore connectivity for shale samples; c. Fractal Dimension and degree of pore connectivity for shale samples.

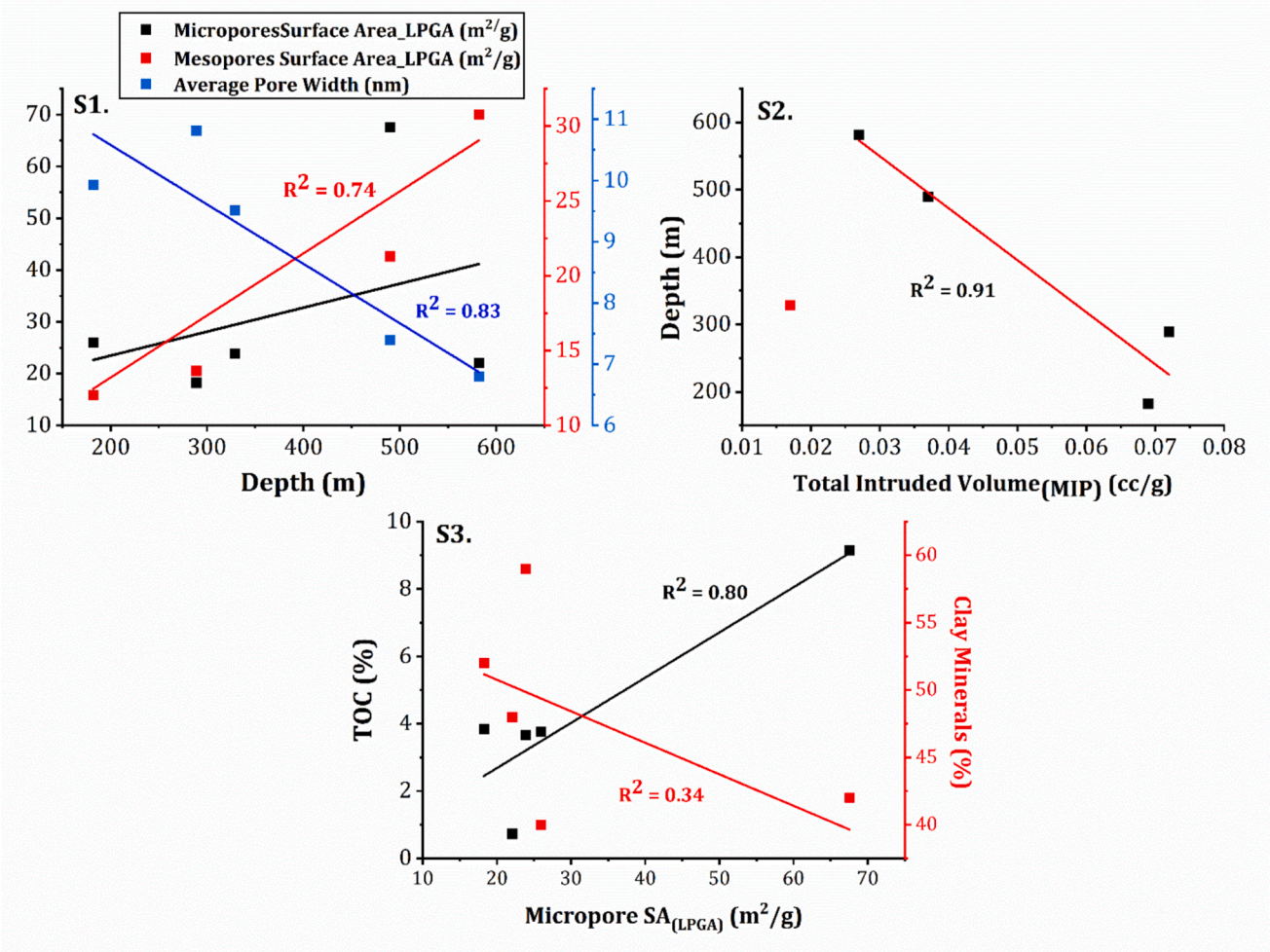

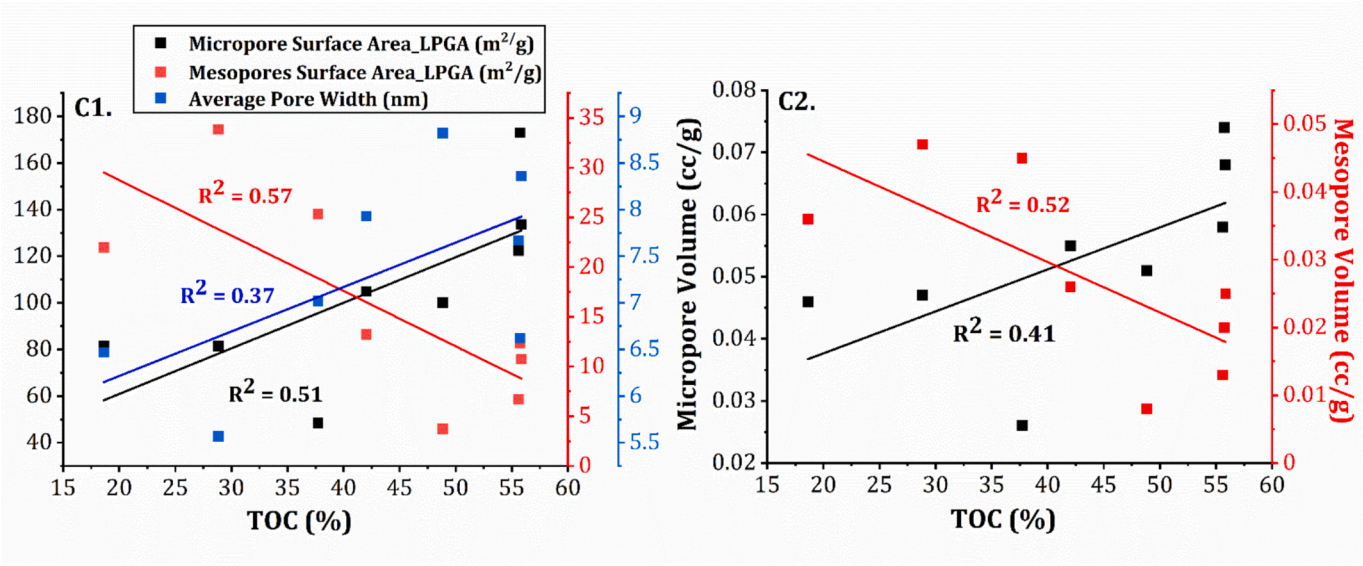

Fig. 12. Correlations between: S1. micropore SA, mesopore SA, and average PW calculated using LPGA method and depth for shale samples; S2. Total Intruded Volume (cc/g) calculated using MICP and depth for shale samples; S3. micropore SA (m^2/g) calculated using the LPGA method and TOC, and clay minerals for shale samples; C1. the micropore SA, mesopore SA, and average PW calculated using the LPGA method, and the TOC for coal samples; C2. micropore volume, and mesopore volume calculated using the LPGA method and TOC for coal samples. C3. Fractal dimension calculated using LPGA and TOC for coal samples; C4. mesopore volume, and total PV calculated using SAXS, and TOC for coal samples.

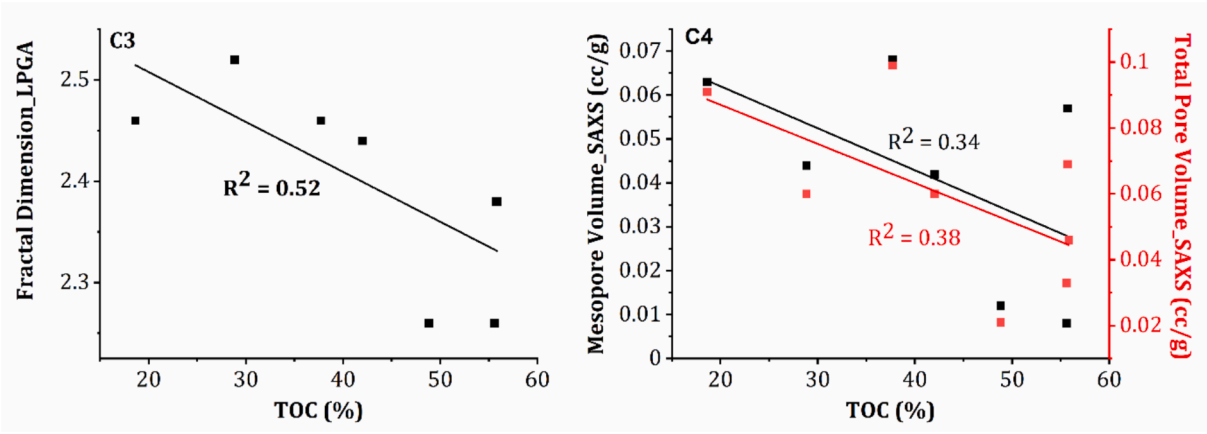

Fig. 12. (*continued*).

high TOC.

4.3. Applicability of microstructural studies on reservoir scale modelling

4.3.1. Pore-Scale modelling

Pore-scale information provides insights into total and effective porosity at the nanoscale, which is crucial for estimating gas storage capacity. It offers details on effective pore connectivity and pore throat, enhancing the understanding of fluid-flow dynamics. SEM images provide information on the pore network and microfracture distribution in coal and shale, offering detailed pore size data with natural fractures and cleats. This contributes to more precise information on pore network models [89,90]. Additionally, SEM images reveal information on surface roughness and mineral composition, which influence wettability and rock-fluid interactions. Sorption properties provide parameters such as Langmuir adsorption isotherms, organic matter, and mineral composition to determine adsorbed and free gas volumes. This improves desorption and diffusion rates through subsurface rock formations, enhancing the estimation of gas storage capacity [91]. Fluid-invasive methods provide data on pore throat compressibility under pressure and changes in pore volume under stress conditions. SEM images depict structural deformation of pores and fractures under applied loads, improving the understanding of pressure-dependent storage capacity [92]. Thus, correlations between organic matter and pore attributes like surface area (SA), pore volume (PV), and surface roughness can be directly applied to pore-scale models. The influence of clay minerals and total organic carbon (TOC) on pore accessibility and connectivity can be integrated into pore-scale models to simulate real fluid migration behavior.

4.3.2. Reservoir-Scale Modelling

Coal and shale formations are heterogeneous with inherently low permeability. Understanding pore connectivity can help address challenges in reservoir-scale simulations. Correlations between surface area and pore connectivity can identify formations or depths that require hydraulic fracturing to enhance pore connectivity. Log data is used to understand reservoir porosity, which primarily reflects macroporosity and natural fractures. Including micropores and mesopores in reservoir models can enhance the accuracy of true storage potential. Clay minerals, such as illite and kaolinite, play a crucial role in exploration and drilling performance. The proportion of swelling clay influences the selection of appropriate drilling fluids and muds during injection [93]. After CO_2 injection, swelling of organic matter reduces permeability, leading to gradual storage capacity loss over time.

5. Conclusion

This study investigates the disparities in pore characteristics between coal and shale samples collected from the Korba Basin in India. The research focuses on their gas storage and production potential in relation to changes in depth, organic composition, and mineral matter content. The key conclusions from this research are as follows:

1. It is evident from gas adsorption analysis that the amount of micropore and mesopore SA in coals is ~ 2.6 and ~ 0.7 times that of shales, respectively. In addition, the total PV of coal sample is 0.30 – 1.5 times that of shale samples depending on their TOC. Furthermore, the amount of micropore volume in coal is 0.95 – 2.6 times of shale, while the amount of mesopores in coal is 0.27 – 0.81 times that of the shale samples. This indicates that the coal sample dominates in micropore volume and surface area compared to the shale samples.
2. The SAXS study identifies both accessible and inaccessible pores in coal and shale, revealing that the meso- and macropore SSA in coal is 0.54–1.16 and 0.41–0.95 times that of the shale samples, respectively, while the mesopore PV is 0.24–1.03 times that of shale samples.
3. Additionally, coal and shale samples exhibit greater pore compression at higher pressure, which helps in assessing variations in pore attributes under high injection pressure conditions. Furthermore, the total SA of coal is 1.02–2.84 times that of the shale samples, while the total PV is 1.74–2.65 times that of the shale samples. This higher SA and total PV can be attributed to the larger pores including natural fractures using the MICP method, which is limited in the LPGA method.
4. The DPC ranges from 0.40 to 0.93 for coal samples and 0.50–0.82 for shale samples. The study observations show that the TOC content and mineral composition in coal and shale sample influence the DPC. In coal samples, high kaolinite content reduces the DPC due to poorly connected pore networks, however fractures with CM can improves the flow pathways. In addition, the micropore SA shows a negative correlation with the DPC. Furthermore, in shale samples, brittle minerals affect the DPC. A lower quartz content in the shale samples enhances the DPC. Thus, the integrated approach to access the pore connectivity provides the valuable understanding on the efficiency of unconventional reservoirs for gas production and storage.
5. Coal samples from the Korba Basin show higher micropore surface area than shale samples, although both coal and shale contain significant amounts of meso- and macropores, making them suitable for CBM and SG recovery. In light of this, a more detailed assessment of these basins should consider additional reservoir parameters.

CRediT authorship contribution statement

Shubham Kumar: Writing – original draft, Visualization, Methodology, Investigation, Formal analysis, Data curation, Conceptualization. **Debanjan Chandra:** Writing – review & editing, Visualization, Validation, Methodology, Investigation, Data curation, Conceptualization. **Bodhisatwa Hazra:** Writing – review & editing, Validation, Investigation. **Vikram Vishal:** Writing – review & editing, Validation, Supervision, Resources, Project administration. **P.G. Ranjith:** Writing – review & editing, Validation. **Anwesa Das:** Writing – review & editing, Validation, Conceptualization. **Mayank Ahuja:** Writing – review & editing, Validation. **Sayan Ghosh:** Writing – review & editing, Supervision, Project administration.

Declaration of competing interest

The authors declare that they have no known competing financial interests or personal relationships that could have appeared to influence the work reported in this paper.

Acknowledgment

The authors acknowledge the Department of Earth Sciences, IITB-Monash Research Academy, and IIT Bombay for the facilities used for the experiments. The authors would like to acknowledge the support from DST, the India-supported National Center of Excellence in Carbon Capture Utilization and Storage (DST/TMD/CCUS/CoE/202/IITB). Shubham Kumar would like to acknowledge the Prime Minister's Research Fellowship (PMRF) from the MHRD, Govt. of India for funding the doctoral program. Authors would also like to acknowledge Sophisticated Analytical Instrumental Facility (SAIF), IITB for SAXS measurements and FEG-SEM imaging.

Appendix A. Supplementary material

Supplementary data to this article can be found online at https://doi.org/10.1016/j.fuel.2025.135185.

Data availability

Data will be made available on request.

References

[1] Meakin P, Huang H, Malthe-Sørenssen A, Thøgersen K. Shale gas: Opportunities and challenges. Environ Geosci 2013;20:151–64. https://doi.org/10.1306/eg.05311313005.
[2] Chandra D, Vishal V, Debbarma A, Banerjee S, Pradhan SP, Mishra MK. Role of Composition and Depth on Pore Attributes of Barakar Formation Gas Shales of Ib Valley, India, Using a Combination of Low-Pressure Sorption and Image Analysis. Energy Fuel 2020. https://doi.org/10.1021/acs.energyfuels.0c00746.
[3] Moore TA. Coalbed methane: A review. Int J Coal Geol 2012;101:36–81. https://doi.org/10.1016/j.coal.2012.05.011.
[4] Vishal V. Recent Advances in Coal Seam Sequestration Research in India - Highlighting Multiphase CO2 Flow for Deep Seam Sequestration. Energy Procedia 2017;114:5377–80. https://doi.org/10.1016/j.egypro.2017.03.1664.
[5] Clarkson CR, Jensen JL, Chipperfield S. Unconventional gas reservoir evaluation: What do we have to consider? J Nat Gas Sci Eng 2012;8:9–33. https://doi.org/10.1016/J.JNGSE.2012.01.001.
[6] Liang W, Yan J, Zhang B, Hou D. Review on Coal Bed Methane Recovery Theory and Technology: Recent Progress and Perspectives. Energy Fuel 2021;35:4633–43. https://doi.org/10.1021/acs.energyfuels.0c04026.
[7] Liu P, Qin Y, Liu S, Hao Y. Numerical Modeling of Gas Flow in Coal Using a Modified Dual-Porosity Model: A Multi-Mechanistic Approach and Finite Difference Method. Rock Mech Rock Eng 2018;51:2863–80. https://doi.org/10.1007/s00603-018-1486-1.
[8] Zhao X, Chen Z, Zhou B, Liao X, Wang H, Wang B. Multiple Flow Mechanism-Based Numerical Model for CO2Huff-n-Puff in Shale Gas Reservoirs with Complex Fractures. Energy Fuel 2023;37:8374–85. https://doi.org/10.1021/acs.energyfuels.3c00931.
[9] Union I, Pure OF, Chemistry A. Recommendations for the characterization of porous solids (Technical Report). Pure Appl Chem 1994;66:1739–58. https://doi.org/10.1351/pac199466081739.
[10] Warren, J E and I P J Root. n.d. 'The Behavior of Naturally Fractured Reservoirs ABSTRACT.' http://onepetro.org/spejournal/article-pdf/3/03/245/2158349/spe-426-pa.pdf/1.
[11] Okeke OC, Okogbue CO. Shales: a Review of Their Classifications, Properties and Importance To the Petroleum Industry. Glob J Geol Sci 2011;9:55–73.
[12] Vishal V, Chandra D, Bahadur J, Sen D, Hazra B, Mahanta B, et al. Interpreting Pore Dimensions in Gas Shales Using a Combination of SEM Imaging, Small-Angle Neutron Scattering, and Low-Pressure Gas Adsorption. Energy Fuel 2019;33:4835–48. https://doi.org/10.1021/acs.energyfuels.9b00442.
[13] Hazra B, Chandra D, Vishal V. Estimation of Gas Storage Capacity Estimate in Coals and Shales 2024. https://doi.org/10.1007/978-3-031-53484-3_3.
[14] Zdravkov A, Bechtel A, Groβ D, Kojić I, Stojanović K, Životić D. Paleovegetation and environment during deposition of the Late Oligocene sub-bituminous coal in the Bobov Dol Basin (SW Bulgaria) as deduced from petrographic and geochemical characteristics. Int J Coal Geol 2024;285. https://doi.org/10.1016/j.coal.2024.104489.
[15] Curry DJ, Emmett JK, Hunt JW. Geochemistry of aliphatic-rich coals in the Cooper Basin, Australia and Taranaki Basin, New Zealand: Implications for the occurrence of potentially oil-generative coals. Geol Soc Spec Publ 1994;77:149–81. https://doi.org/10.1144/GSL.SP.1994.077.01.09.
[16] Wang M, Xue H, Tian S, Wilkins RWT, Wang Z. Fractal characteristics of Upper Cretaceous lacustrine shale from the Songliao Basin. NE China Mar Pet Geol 2015;67:144–53. https://doi.org/10.1016/j.marpetgeo.2015.05.011.
[17] Liu Y, Zhu Y. Comparison of pore characteristics in the coal and shale reservoirs of Taiyuan Formation, Qinshui Basin. China Int J Coal Sci Technol 2016;3:330–8. https://doi.org/10.1007/s40789-016-0143-0.
[18] Ju Y, Sun Y, Tan J, Bu H, Han K, Li X, et al. The composition, pore structure characterization and deformation mechanism of coal-bearing shales from tectonically altered coalfields in eastern China. Fuel 2018;234:626–42. https://doi.org/10.1016/j.fuel.2018.06.116.
[19] Liu B, Mohammadi MR, Ma Z, Bai L, Wang L, Xu Y, et al. Evolution of porosity in kerogen type I during hydrous and anhydrous pyrolysis: Experimental study, mechanistic understanding, and model development. Fuel 2023:338. https://doi.org/10.1016/j.fuel.2022.127149.
[20] Wang Z, Fu X, Hao M, Li G, Pan J, Niu Q, et al. Experimental insights into the adsorption-desorption of CH4/N2 and induced strain for medium-rank coals. J Pet Sci Eng 2021;204:108705. https://doi.org/10.1016/j.petrol.2021.108705.
[21] Zhang T, Ellis GS, Ruppel SC, Milliken K, Yang R. Effect of organic-matter type and thermal maturity on methane adsorption in shale-gas systems. Org Geochem 2012;47:120–31. https://doi.org/10.1016/j.orggeochem.2012.03.012.
[22] Curtis ME, Ambrose RJ, Sondergeld CH, Rai CS. Investigation of the relationship between organic porosity and thermal maturity in the Marcellus Shale. Soc Pet Eng - SPE Am Unconv Gas Conf 2011, UGC 2011 2011:764–7. https://doi.org/10.2118/144370-ms.
[23] Hazra B, Chandra D, Singh AK, Varma AK, Mani D, Singh PK, et al. Comparative pore structural attributes and fractal dimensions of Lower Permian organic-matter-bearing sediments of two Indian basins: Inferences from nitrogen gas adsorption. Energy Sources, Part A Recover Util Environ Eff 2019;41:2975–88. https://doi.org/10.1080/15567036.2019.1582737.
[24] Ross DJK, Marc BR. The importance of shale composition and pore structure upon gas storage potential of shale gas reservoirs. Mar Pet Geol 2009;26:916–27. https://doi.org/10.1016/j.marpetgeo.2008.06.004.
[25] Jarvie DM. Shale resource systems for oil and gas: Part 2—shale-oil resource systems. AAPG Mem 2012;97:89–119. https://doi.org/10.1306/13321447M973489.
[26] Gonzalez R, Schepers K, Riestenberg D, Koperna G, Oudinot A. Assessment of the potential and economic performance for ECBM recovery and CO2 sequestration. SPE Lat Am Caribb Pet Eng Conf Proc 2009;1:196–225. https://doi.org/10.2118/121157-ms.
[27] Chandra D, Vishal V. A Comparative Analysis of Pore Attributes of Sub-Bituminous Gondwana Coal from the Damodar and Wardha Valleys: Implication for Enhanced Coalbed Methane Recovery. Energy Fuel 2022. https://doi.org/10.1021/acs.energyfuels.2c00854.
[28] Hazra B, Varma AK, Bandopadhyay AK, Mendhe VA, Singh BD, Saxena VK, et al. Petrographic insights of organic matter conversion of Raniganj basin shales. India Int J Coal Geol 2015;150–151:193–209. https://doi.org/10.1016/j.coal.2015.09.001.
[29] Chandra D, Bakshi T, Vishal V. Thermal effect on pore characteristics of shale under inert and oxic environments: Insights on pore evolution. Microporous Mesoporous Mater 2021;316:110969. https://doi.org/10.1016/j.micromeso.2021.110969.
[30] Radlinski AP, Mastalerz M, Hinde AL, Hainbuchner M, Rauch H, Baron M, et al. Application of SAXS and SANS in evaluation of porosity, pore size distribution and surface area of coal. Int J Coal Geol 2004;59:245–71. https://doi.org/10.1016/j.coal.2004.03.002.
[31] Chalmers GR, Bustin RM, Power IM. Characterization of gas shale pore systems by porosimetry, pycnometry,surfacearea,andfield emission scanning electron microscopy/ transmission electron microscopy image analyses: Examples from the Barnett, Woodford, Haynesville, Marcellus,andDoig units. Am Assoc Pet Geol Bull 2012;96:1099–119. https://doi.org/10.1306/10171111052.
[32] Mastalerz M, He L, Melnichenko YB, Rupp JA. Porosity of coal and shale: Insights from gas adsorption and SANS/USANS techniques. Energy Fuel 2012;26:5109–20. https://doi.org/10.1021/ef300735t.

[33] Sang G, Liu S, Zhang R, Elsworth D, He L. Nanopore characterization of mine roof shales by SANS, nitrogen adsorption, and mercury intrusion: Impact on water adsorption/retention behavior. Int J Coal Geol 2018;200:173–85. https://doi.org/10.1016/j.coal.2018.11.009.
[34] Chandra D, Bakshi T, Bahadur J, Hazra B, Vishal V, Kumar S, et al. Pore morphology in thermally-treated shales and its implication on CO2 storage applications: A gas sorption, SEM, and small-angle scattering study. Fuel 2023;331:125877. https://doi.org/10.1016/j.fuel.2022.125877.
[35] Sun Z, Li X, Liu W, Zhang T, He M, Nasrabadi H. Molecular dynamics of methane flow behavior through realistic organic nanopores under geologic shale condition: Pore size and kerogen types. Chem Eng J 2020;398:124341. https://doi.org/10.1016/j.cej.2020.124341.
[36] Ma Z, Ranjith PG. Review of application of molecular dynamics simulations in geological sequestration of carbon dioxide. Fuel 2019:255. https://doi.org/10.1016/j.fuel.2019.115644.
[37] Wu T, Firoozabadi A. Effect of Microstructural Flexibility on Methane Flow in Kerogen Matrix by Molecular Dynamics Simulations. J Phys Chem C 2019;123:10874–80. https://doi.org/10.1021/acs.jpcc.8b12328.
[38] Anovitz LM, Cole DR. Characterization and analysis of porosity and pore structures. Pore Scale Geochemical Process. De Gruyter 2015:61–164. https://doi.org/10.2138/rmg.2015.80.04.
[39] Liu S, Xue H, Zhao M. Pore Structure and Fractal Characteristics of Coal Measure Shale in the Wuxiang Block in the Qinshui Basin. Processes 2023;11. https://doi.org/10.3390/pr11123362.
[40] Hazra B, Chandra D, Vishal V. Unconventional Hydrocarbon Reservoirs: Coal and Shale. 2024. Doi:10.1007/978-3-031-53484-3.
[41] Geological Survey of India, 2005, District Resource MAP of Korba, Chhattisgarh. https://employee.gsi.gov.in/cs/groups/public/documents/document/b3zp/otex/~edisp/dcport1gsigovi911919.jpg.
[42] Kumar S, Chandra D, Hazra B, Vishal V, Pathegama GR. Nanopore Characteristics of Barakar Formation Shales and Their Impact on the Gas Storage Potential of Korba and Raniganj Basins in India. Energy Fuel 2024. https://doi.org/10.1021/acs.energyfuels.3c03374.
[43] Singh KJ, Saxena A, Goswami S. Palaeobiodiversity of the Lower Gondwana rocks in the Korba Coalfield, Chhattisgarh, India and observations on the genus Gangamopteris McCoy. J Palaeosciences 2012;61:145–63. https://doi.org/10.54991/jop.2012.356.
[44] Tewari RC, Hota RN, Maejima W. Fluvial architecture of Early Permian Barakar rocks of Korba Gondwana basin, eastern-central India. J Asian Earth Sci 2012;52:43–52. https://doi.org/10.1016/j.jseaes.2012.02.009.
[45] Mukhopadhyay G, Mukhopadhyay SK, Roychowdhury M, Parui PK. Stratigraphic correlation between different Gondwana Basins of India. J Geol Soc India 2010;76:251–66. https://doi.org/10.1007/s12594-010-0097-6.
[46] Mastalerz M, Schimmelmann A, Drobniak A, Chen Y. Porosity of Devonian and Mississippian New Albany Shale across a maturation gradient: Insights from organic petrology', gas adsorption, and mercury intrusion. Am Assoc Pet Geol Bull 2013;97:1621–43. https://doi.org/10.1306/04011312194.
[47] Ward CR, Taylor JC, Matulis CE, Dale LS. Quantification of mineral matter in the Argonne Premium Coals using interactive Rietveld-based X-ray diffraction. vol. 46. 2001.
[48] Ruan C-D, Ward CR. Quantitative X-ray powder diffraction analysis of clay minerals in Australian coals using Rietveld methods. n.d.
[49] Ritz M, Klika Z. Determination of minerals in coal by methods based on the recalculation of the bulk chemical analyses. vol. 7. 2010.
[50] Hazra B, Chandra D, Vishal V. Imaging and Visualization 2024:73–100. https://doi.org/10.1007/978-3-031-53484-3_4.
[51] Hazra B, Wood DA, Singh PK, Singh AK, Kumar OP, Raghuvanshi G, et al. Source rock properties and pore structural framework of the gas-prone Lower Permian shales in the Jharia basin, India. Arab J Geosci 2020;13. https://doi.org/10.1007/s12517-020-05515-3.
[52] Hazra B, Vishal V, Singh DP. Applicability of Low-Pressure CO2 and N2 Adsorption in Determining Pore Attributes of Organic-Rich Shales and. Coals 2020. https://doi.org/10.1021/acs.energyfuels.0c03412.
[53] Chandra D, Bakshi T, Bahadur J, Hazra B, Vishal V, Kumar S, et al. Pore morphology in thermally-treated shales and its implication on CO2 storage applications: A gas sorption, SEM, and small-angle scattering study. Fuel 2023;331:125877. https://doi.org/10.1016/J.FUEL.2022.125877.
[54] Feng G, Li W, Zhu Y, Wang Y, Song Y, Zheng S, et al. Scale-Dependent Fractal Properties and Geological Factors for the Pore Structure in Shale: Insights from Field Emission Scanning Electron Microscopy and Fluid Intrusion. Energy Fuel 2023;37:16519–35. https://doi.org/10.1021/acs.energyfuels.3c02833.
[55] Liu Y, Zhu Y. Comparison of pore characteristics in the coal and shale reservoirs of Taiyuan Formation, Qinshui Basin, China. Int J Coal Sci Technol 2016;3:330–8. https://doi.org/10.1007/s40789-016-0143-0.
[56] Léon Y, León CA. New perspectives in mercury porosimetry. Adv Colloid Interface Sci 1998;76–77:341–72. https://doi.org/10.1016/S0001-8686(98)00052-9.
[57] Washburn EW. The Dynamics of Capillary Flow. Physical Review 1921;17:273–83. https://doi.org/10.1103/PhysRev.17.273.
[58] Diamond S. Mercury porosimetry: an inappropriate method for the measurement of pore size distributions in cement-based materials. Cem Concr Res 2000;30:1517–25. https://doi.org/10.1016/S0008-8846(00)00370-7.
[59] Chandra D, Vishal V, Bahadur J, Sen D. A novel approach to identify accessible and inaccessible pores in gas shales using combined low-pressure sorption and SAXS/SANS analysis. Int J Coal Geol 2020:228. https://doi.org/10.1016/j.coal.2020.103556.
[60] Rezaeyan A, Pipich V, Busch A. MATSAS: A small-angle scattering computing tool for porous systems. J Appl Crystallogr 2021;54:697–706. https://doi.org/10.1107/S1600576721000674.
[61] Zhang S, Tang S, Tang D, Huang W, Pan Z. Determining fractal dimensions of coal pores by FHH model: Problems and effects. J Nat Gas Sci Eng 2014;21:929–39. https://doi.org/10.1016/j.jngse.2014.10.018.
[62] Liu K, Ostadhassan M, Jang HW, Zakharova NV, Shokouhimehr M. Comparison of fractal dimensions from nitrogen adsorption data in shale: via different models. RSC Adv 2021;11:2298–306. https://doi.org/10.1039/d0ra09052b.
[63] Sastry PU, Sen D, Mazumder S, Chandrasekaran KS. Structural variations in lignite coal: A small angle X-ray scattering investigation. Solid State Commun 2000;114:329–33. https://doi.org/10.1016/S0038-1098(00)00060-0.
[64] Niu Q, Pan J, Jin Y, Wang H, Li M, Ji Z, et al. Fractal study of adsorption-pores in pulverized coals with various metamorphism degrees using N2 adsorption, X-ray scattering and image analysis methods. J Pet Sci Eng 2019;176:584–93. https://doi.org/10.1016/j.petrol.2019.01.107.
[65] Feng G, Li W, Zhu Y, Wang Y, Song Y, Zheng S, et al. Scale-Dependent Fractal Properties and Geological Factors for the Pore Structure in Shale: Insights from Field Emission Scanning Electron Microscopy and Fluid Intrusion. Energy Fuel 2023;37:16519–35. https://doi.org/10.1021/acs.energyfuels.3c02833.
[66] Liu J, Zhu Y, Li S, Feng G. Response of Coal Nanopores and Their Complexity to Igneous Intrusion. Energy Fuel 2024;38:2969–82. https://doi.org/10.1021/acs.energyfuels.3c04213.
[67] Jiao K, Yao S, Liu C, Gao Y, Wu H, Li M, et al. The characterization and quantitative analysis of nanopores in unconventional gas reservoirs utilizing FESEM-FIB and image processing: An example from the lower Silurian Longmaxi Shale, upper Yangtze region. China Int J Coal Geol 2014;128–129:1–11. https://doi.org/10.1016/j.coal.2014.03.004.
[68] Löhr SC, Baruch ET, Hall PA, Kennedy MJ. Is organic pore development in gas shales influenced by the primary porosity and structure of thermally immature organic matter? Org Geochem 2015;87:119–32. https://doi.org/10.1016/j.orggeochem.2015.07.010.
[69] Peng S, Yang J, Xiao X, Loucks B, Ruppel SC, Zhang T. An Integrated Method for Upscaling Pore-Network Characterization and Permeability Estimation: Example from the Mississippian Barnett Shale. Transp Porous Media 2015;109:359–76. https://doi.org/10.1007/s11242-015-0523-8.
[70] Loucks RG, Reed RM, Ruppel SC, Hammes U. Spectrum of pore types and networks in mudrocks and a descriptive classification for matrix-related mudrock pores. Am Assoc Pet Geol Bull 2012;96:1071–98. https://doi.org/10.1306/08171111061.
[71] Loucks RG, Reed RM. Scanning-electron-microscope petrographic evidence for distinguishing organic-matter pores associated with depositional organic matter versus migrated organic matter in mudrocks. GCAGS J 2014;3:51–60.
[72] Ivanić M, Vdović N, Barreto SDB, Bermanec V, Sondi I. Mineralogy, surface properties and electrokinetic behaviour of kaolin clays derived from naturally occurring pegmatite and granite deposits. Geol Croat 2015;68:139–45. https://doi.org/10.4154/gc.2015.09.
[73] Mosher K, He J, Liu Y, Rupp E, Wilcox J. Molecular simulation of methane adsorption in micro- and mesoporous carbons with applications to coal and gas shale systems. Int J Coal Geol 2013;109–110:36–44. https://doi.org/10.1016/j.coal.2013.01.001.
[74] Groen JC, Peffer LAA, Pérez-Ramírez J. Pore size determination in modified micro- and mesoporous materials. Pitfalls and limitations in gas adsorption data analysis. Microporous Mesoporous Mater 2003;60:1–17. https://doi.org/10.1016/S1387-1811(03)00339-1.
[75] Liu X, Xiong J, Liang L. Investigation of pore structure and fractal characteristics of organic-rich Yanchang formation shale in central China by nitrogen adsorption/desorption analysis. J Nat Gas Sci Eng 2015;22:62–72. https://doi.org/10.1016/j.jngse.2014.11.020.
[76] Bhapkar PV, Pradhan SP, Chandra D, Hazra B, Vishal V. Systematic Pore Characterization of Sub-Bituminous Coal from Sohagpur Coalfield, Central India Using Gas Adsorption Coupled with X-ray Scattering and High-Resolution Imaging. Energy Fuel 2023;37:9297–308. https://doi.org/10.1021/acs.energyfuels.3c01007.
[77] Zhao D, Guo Y, Wang G, Guan X, Zhou X, Liu J. Fractal Analysis and Classification of Pore Structures of High-Rank Coal in Qinshui Basin. China Energies 2022;15. https://doi.org/10.3390/en15186766.
[78] Li Y, Song D, Liu S, Ji X, Hao H. Evaluation of pore properties in coal through compressibility correction based on mercury intrusion porosimetry: A practical approach. Fuel 2021;291:120130. https://doi.org/10.1016/j.fuel.2021.120130.
[79] Feng G, Li W, Zhu Y, Wang X, Wang Y, Song Y, et al. Matrix Compressibility and Multifractal Nature of Nanoporous Shale. Energy Fuel 2024;38:4057–75. https://doi.org/10.1021/acs.energyfuels.3c04830.
[80] Rouquerol F, Rouquerol J, Sing KSW, Llewellyn P, Maurin G, York N, et al. Adsorption by Powders and Porous Solids Principles, Methodology and Applications Second edition. 2014.
[81] Yu Y, Luo X, Wang Z, Cheng M, Lei Y, Zhang L, et al. A new correction method for mercury injection capillary pressure (MICP)to characterize the pore structure of shale. J Nat Gas Sci Eng 2019;68:102896. https://doi.org/10.1016/j.jngse.2019.05.009.
[82] Sing K. The use of nitrogen adsorption for the characterisation of porous materials. Colloids Surfaces A Physicochem Eng Asp 2001;187–188:3–9. https://doi.org/10.1016/S0927-7757(01)00612-4.
[83] Thommes M. Physical Adsorption Characterization of Ordered and Amorphous Mesoporous Materials 2004:317–64. Doi:10.1142/9781860946561_0011.
[84] Zhao F, Dong Z, Wang C, Zhang W, Yu R. Pore Connectivity Characteristics and Controlling Factors for Black Shales in the Wufeng-Longmaxi Formation,

Southeastern Sichuan Basin, China. Energies 2022;15. https://doi.org/10.3390/en15082909.
[85] Sun M, Duan X, Liu Q, Blach TP, Ostadhassan M, Liu B, et al. The importance of pore-fracture connectivity in overmature marine shale for methane occurrence and transportation. Mar Pet Geol 2023;157:106495. https://doi.org/10.1016/j.marpetgeo.2023.106495.
[86] Okolo GN, Everson RC, Neomagus HWJP, Roberts MJ, Sakurovs R. Comparing the porosity and surface areas of coal as measured by gas adsorption, mercury intrusion and SAXS techniques. Fuel 2015;141:293–304. https://doi.org/10.1016/j.fuel.2014.10.046.
[87] Vishal V, Singh TN, Ranjith PG. Influence of sorption time in CO2-ECBM process in Indian coals using coupled numerical simulation. Fuel 2015;139:51–8. https://doi.org/10.1016/j.fuel.2014.08.009.
[88] Yu S, Bo J, Fengli L, Jiegang L. Structure and fractal characteristic of micro- and meso-pores in low, middle-rank tectonic deformed coals by CO2 and N2 adsorption. Microporous Mesoporous Mater 2017;253:191–202. https://doi.org/10.1016/j.micromeso.2017.07.009.
[89] Feng J, Xiong Q, Qu Y, Yang D. A new dual-scale pore network model with triple-pores for shale gas simulation. Geoenergy Sci Eng 2024;235:212710. https://doi.org/10.1016/j.geoen.2024.212710.
[90] Jing Y, Rabbani A, Armstrong RT, Wang J, Mostaghimi P. A hybrid fracture-micropore network model for multiphysics gas flow in coal. Fuel 2020;281:118687. https://doi.org/10.1016/j.fuel.2020.118687.
[91] Li J, Lu S, Zhang P, Cai J, Li W, Wang S, et al. Estimation of gas-in-place content in coal and shale reservoirs: A process analysis method and its preliminary application. Fuel 2020;259:116266. https://doi.org/10.1016/j.fuel.2019.116266.
[92] Li X, Wang J, Li Z, Zhang K, Feng X, Wang Z. Impact of Brittle Deformation on Pore Structure Evolution in Shale: Samples Collected from Different Fault Positions. Energy and Fuels 2022;36:1441–56. https://doi.org/10.1021/acs.energyfuels.1c03808.
[93] Zhang JR, Xu MD, Christidis GE, Zhou CH. Clay minerals in drilling fluids: functions and challenges. Clay Miner 2020;55:1–11. https://doi.org/10.1180/clm.2020.10.